

# Insights on Muon from Simple Quadratics

Antoine Gonon

Andreea-Alexandra Mușat

Nicolas Boumal

Institute of Mathematics, EPFL, Switzerland

## Abstract

MUON updates weight matrices along (approximate) polar factors of the gradients and has shown strong empirical performance in large-scale training. Existing attempts at explaining its performance largely focus on single-step comparisons (on quadratic proxies) and worst-case guarantees that treat the inexactness of the polar-factor as a nuisance “to be argued away”. We show that already on simple strongly convex functions such as  $L(W) = \frac{1}{2}\|W\|_F^2$ , these perspectives are insufficient, suggesting that understanding MUON requires going beyond local proxies and pessimistic worst-case bounds. Instead, our analysis exposes two observations that already affect behavior on simple quadratics and are not well captured by prevailing abstractions: (i) approximation error in the polar step can qualitatively alter discrete-time dynamics and *improve* reachability and finite-time performance—an effect practitioners exploit to tune MUON, but that existing theory largely treats as a pure accuracy compromise; and (ii) structural properties of the objective affect finite-budget constants beyond the prevailing conditioning-based explanations. Thus, any general theory covering these cases must either incorporate these ingredients explicitly or explain why they are irrelevant in the regimes of interest.

**Code.** [github.com/agonon/muon-on-quadratics](https://github.com/agonon/muon-on-quadratics).

## 1 Introduction

MUON (MomentUm Orthogonalized by Newton–Schulz) has gained attention as an optimizer for large language models by improving training speed on GPT-style models [Jordan \[2024\]](#), [Liu et al. \[2025\]](#), [Shah et al. \[2025\]](#). At a high level, MUON can be viewed as SGD with Nesterov-momentum, except that instead of taking a step directly in the direction of the momentum matrix, it first approximately orthogonalizes it using a small number of Newton–Schulz (polynomial) iterations. These iterations approximate the polar factor (equivalently, a matrix-sign map), resulting in an update direction that lies approximately on the Stiefel manifold before a standard step is taken [Jordan \[2024\]](#). Code is provided in Section A.

This design has motivated a growing theoretical literature that views MUON-style updates through the lens of spectral-norm steepest descent and linear minimization oracles, and studies convergence under smoothness assumptions with various idealizations such as exact orthogonalization, non-Nesterov momentum, simplified step-size rules, and locally quadratic models [Pethick et al. \[2025\]](#), [Li and Hong \[2025\]](#), [Shen et al. \[2025\]](#), [Chen et al. \[2025\]](#), [Kovalev \[2025\]](#), [Riabinin et al. \[2025\]](#), [Gruntkowska et al. \[2025\]](#), [Sato et al. \[2025\]](#), [Nagashima and Iiduka \[2026\]](#). More recent work begins to incorporate *inexact* polar steps and quantify how approximation error propagates in worst-case bounds [Shulgin et al. \[2025\]](#), [Kim and Oh \[2026\]](#), [Lau et al. \[2025\]](#).

Despite this progress, it remains unclear what parts of MUON’s behavior are explained by these idealized viewpoints. Two themes in particular recur across the literature and practitioner discussions: (i) analyses that emphasize quadratic or locally quadratic behavior and per-step improvement along a spectral/Stiefel direction, and (ii) analyses that treat projection inexactness primarily as a computational cost–accuracy tradeoff. These themes naturally lead to several basic questions that are not settled by existing results.

**Q1: Does MUON actually find the global minimizer of a smooth, strongly convex function?** Many guarantees for MUON-like methods target stationarity measures over general smooth objectives [Pethick et al. \[2025\]](#), [Li and Hong \[2025\]](#), [Shen et al. \[2025\]](#), [Chen et al. \[2025\]](#), [Kovalev \[2025\]](#), [Riabinin et al. \[2025\]](#), [Gruntkowska et al. \[2025\]](#), [Sato et al. \[2025\]](#), [Shulgin et al. \[2025\]](#), [Kim and Oh \[2026\]](#), [Lau et al. \[2025\]](#), [Nagashima and Iiduka \[2026\]](#). These analyses rely on tools from optimization theory (e.g., descent lemmas) that are most effective under strong convexity assumptions. But what if we *do* have strong convexity? Can we already guarantee basic properties such as convergence to the global minimizer?

And more quantitatively, what advantage does MUON offer over standard methods such as GD in terms of convergence speed to a given loss level?

**Q2: Ignoring computational cost, is an exact polar factorization always preferable to an approximate one, or can approximations *improve* optimization dynamics?** A common modeling choice treats inexactness as an error term that monotonically worsens a baseline method [Shulgin et al. \[2025\]](#), [Kim and Oh \[2026\]](#), [Lau et al. \[2025\]](#), and much numerical work aims to reduce approximation error for a fixed compute budget [Amsel et al. \[2025\]](#), [Cesista et al. \[2025\]](#), [Grishina et al. \[2025\]](#), [Boumal and Gonon \[2025\]](#). Yet MUON’s practical implementation *deliberately* uses low-degree approximations whose errors are not negligible. Is approximation merely an implementation compromise, or can projection inexactness qualitatively change the discrete-time dynamics in a way that can *help* reach small-loss regimes?

**Q3: Is it appropriate to assess MUON by comparing it to competing algorithms one iteration at a time?** Several analyses compare the per-step decrease obtained by the polar/Stiefel direction to that of the Euclidean gradient direction under line-search optimal step sizes or quadratic proxies [Davis and Drusvyatskiy \[2025\]](#), [Su \[2025\]](#). Does local, “greedy” superiority translate into a global convergence?

**Contributions.** We provide a few answers:

**A1: For MUON to minimize even a strongly convex loss, its step sizes must vanish—this is not the default (Section 3).** We exhibit strongly convex losses where, under constant step sizes and exact projection, the dynamics become confined to discrete lattices (“grid confinement”): for almost all initializations, the iterates never enter sufficiently small loss balls. Moreover, even in favorable (reachable) cases, the best possible iteration count to reach loss  $\varepsilon$  is  $O(1/\sqrt{\varepsilon})$ , in contrast with GD’s  $O(\log(1/\varepsilon))$  on the same objective. Thus, MUON has no advantage in the asymptotic  $\varepsilon$ -dependence. Beyond asymptotic rates, we analyze whether finite-time speedups can arise through more favorable big-O constants in ill-conditioned settings, a prevailing hypothesis behind MUON’s practical success [Jordan \[2024\]](#). While such effects appear in worst-case constructions, we show that in typical quadratic instances, the conditioning alone does not explain finite-budget performance. Rather, finer spectral properties such as spectrum shape also matter.

**A2: Inexact projection is not just a nuisance (Section 4).** On a simple quadratic, introducing stochastic perturbations to the polar step restores eventual reachability of small-loss neighborhoods and can reduce the iteration count required to reach a given loss level. That count is not a monotone function of the perturbation magnitude: an intermediate noise level yields the fastest convergence on this toy model. This demonstrates that, even in a simplified error model, inexact projection can play a constructive algorithmic role rather than acting solely as a computational compromise. For the Newton–Schulz approximation used in practice, experiments on quadratics show that approximation error can either accelerate or slow convergence depending on the spectral structure of the loss, highlighting that approximation error plays a role beyond a simple cost-accuracy tradeoff.

**A3: One-step superiority can be globally misleading (Section 5).** We entertain a greedy policy which, at each step, picks the best update between a gradient step or a Stiefel/polar step, both with their optimal step size. We exhibit general quadratics such that it is always the Stiefel/polar step that is picked, yet the GD trajectory overall is much faster. This shows that per-iteration comparisons are not a reliable proxy for end-to-end convergence speed.

**Take-home message.** Even on simple strongly convex quadratics, MUON exhibits non-trivial discrete-time behavior that already acts as a filter as to which explanatory narratives can be universally meaningful. In particular, our analysis challenges two common viewpoints, stating instead: (i) local one-step superiority arguments are not reliable predictors of end-to-end speed, and (ii) worst-case guarantees that degrade monotonically with polar approximation error do not qualitatively capture the role of inexact projection.

At the same time, this work brings forward two ingredients that are quite overlooked in existing theory but that must be confronted by any general explanation of MUON’s behavior. First, approximation error in the polar step can play a constructive role by accelerating convergence. Second, while MUON does not improve worst-case asymptotic  $\varepsilon$ -dependence on convex objectives, our quadratic experiments show that any advantage must come from problem-dependent big-O constants rather than asymptotic rates. A prevailing hypothesis behind MUON’s practical success is a form of conditioning insensitivity: since GD’s worst-case guarantees deteriorate with the condition number  $\kappa$ , one might expect MUON to win systematically on poorly conditioned problems. However, this worst-case dependence of GD on  $\kappa$  is not

representative of typical quadratic behavior, where performance depends on finer spectral properties beyond  $\kappa$  alone. In our controlled setting, conditioning alone is therefore not predictive: at fixed  $\kappa$ , changing the spectrum shape can flip whether MUON beats GD. Moreover, MUON’s loss decrease is comparatively stable across the spectrum families we test, so the variation in who wins is largely driven by GD’s sensitivity to finer spectral structure.

## 2 Related Work

A few *recurring methodological lenses* have shaped the current understanding of MUON-like methods. Existing theoretical work either (i) analyzes MUON-like updates through smoothness-based descent arguments and norm-constrained subproblems, or (ii) motivates MUON-like directions via per-iteration improvement on quadratic proxies. In parallel, numerical work on polar approximations largely treats inexactness as a cost–accuracy knob. We review these threads through the three aspects we focus on: strong convexity, one-step comparisons, and the role of inexact projection.

**MUON as approximate orthogonalization of momentum.** Muon (code in Section A) combines (i) maintaining a Nesterov-style momentum matrix and (ii) applying a small number of GPU-friendly Newton–Schulz / polynomial steps that approximate its polar factor (matrix sign), yielding an update direction that lies approximately on the Stiefel manifold, before a standard step is taken [Jordan \[2024\]](#). We use the implementation of the nanoGPT speedrun benchmark as a reference point since it keeps track of the latest practical choices that matter for state-of-the-art performance [Jordan et al. \[2024\]](#). In particular, we will see that a theoretical challenge posed by this implementation is that it uses non-vanishing step sizes (see Section 3), even though this implies inherent obstructions to convergence already on simple strongly convex functions. Subsequent empirical studies explore how MUON compares to AdamW and SGD-momentum across architectures and scales, and how implementation choices such as normalization, weight decay, learning-rate schedules, and the number/degree of polar steps affect outcomes [Liu et al. \[2025\]](#), [Shah et al. \[2025\]](#). These empirical works make it clear that MUON is defined not only by a direction (polar/Stiefel) but by a well-tuned combination of step-size, momentum, and projection inexactness, which motivates asking which components are essential for qualitative behavior.

**Smoothness-based analyses via norm-constrained subproblems and descent lemmas.** A large body of theoretical work studies MUON updates by interpreting them as solutions of spectral-norm constrained subproblems that would be solved at each gradient step (LMOs, steepest descent in non-Euclidean norms, or related trust-region steps). The same works then apply standard smoothness tools (descent lemmas based on Lipschitz gradients) to derive worst-case guarantees over general smooth objectives [Pethick et al. \[2025\]](#), [Li and Hong \[2025\]](#), [Shen et al. \[2025\]](#), [Chen et al. \[2025\]](#), [Kovalev \[2025\]](#), [Riabinin et al. \[2025\]](#), [Gruntkowska et al. \[2025\]](#), [Sato et al. \[2025\]](#), [Nagashima and Iiduka \[2026\]](#). A representative object is the linear minimization oracle for a norm  $\|\cdot\|$ ,

$$\text{LMO}(D) \in \operatorname{argmin}_{\|V\| \leq 1} \langle D, V \rangle,$$

for which the spectral-norm LMO is given by the negative polar factor  $-UV^\top$  when  $D = USV^\top$  is an SVD [Pethick et al. \[2025\]](#). This is precisely the matrix-sign / polar-factor direction that MUON approximates.

These analyses typically yield *stationarity-type* conclusions under standard assumptions (Lipschitz gradients, access to unbiased stochastic gradients with bounded variance), and often consider idealized update rules (exact projection, no momentum or non-Nesterov momentum, and simplified step-size rules such as vanishing ones) [Pethick et al. \[2025\]](#), [Li and Hong \[2025\]](#), [Shen et al. \[2025\]](#), [Chen et al. \[2025\]](#), [Kovalev \[2025\]](#), [Riabinin et al. \[2025\]](#), [Gruntkowska et al. \[2025\]](#), [Sato et al. \[2025\]](#), [Nagashima and Iiduka \[2026\]](#). Because the underlying toolkit is built around smoothness and descent, it is natural to ask what these guarantees imply in the most favorable setting these tools have been designed for—*strong convexity*. This leads directly to **Q1**: if we *do* have a smooth, strongly convex objective, does MUON necessarily converge to the global minimizer in discrete time under standard (non-vanishing, as in the nanoGPT speedrun contest [Jordan et al. \[2024\]](#)) step sizes? What is the best possible asymptotic dependence of the time-to- $\varepsilon$  loss on  $\varepsilon$ ?

**Quadratic proxies and one-step improvement arguments.** A separate thread uses quadratic or locally quadratic models to justify when spectral/Stiefel directions should offer better *one-step* decrease than Euclidean gradients, often emphasizing conditioning and alignment effects [Davis and Drusvyatskiy \[2025\]](#), [Su \[2025\]](#). This perspective is compelling because it connects MUON-style directions to an interpretable per-iteration metric. At the same time, it naturally raises **Q3**: is it appropriate to assess

MUON by comparing it to competing algorithms one iteration at a time? In particular, does greedy one-step superiority reliably translate into faster end-to-end convergence along the full trajectory?

**Inexact projection.** Muon’s projection is an approximate polar decomposition / matrix-sign computation implemented with a small number of Newton–Schulz-like or polynomial iterations. A rapidly growing literature aims at improving these approximations for a fixed compute budget, including polynomial design, stability/precision engineering [Amsel et al. \[2025\]](#), [Grishina et al. \[2025\]](#), [Cesista et al. \[2025\]](#), [Lau et al. \[2025\]](#), [Boumal and Gonon \[2025\]](#), [Kang et al. \[2025\]](#). These approaches mainly treat approximation quality as a cost–accuracy knob.

On the theory side, recent works begin to model *inexact* LMOs / inexact polar steps and track how an error parameter propagates through worst-case bounds [Shulgin et al. \[2025\]](#), [Kim and Oh \[2026\]](#), [Lau et al. \[2025\]](#). This is an important step toward realism, but the prevailing abstraction still treats inexactness as a nuisance term that monotonically worsens guarantees relative to the exact-projection baseline.

Muon’s practice, however, deliberately operates in a regime where the polar step is low-degree and the error is not negligible [Jordan \[2024\]](#), [Liu et al. \[2025\]](#), [Shah et al. \[2025\]](#). Moreover, several works explicitly tune approximation mechanisms to improve optimization speed rather than to minimize approximation error per se [Ahn et al. \[2025\]](#), [Khaled et al. \[2025\]](#), [He et al. \[2025\]](#). This naturally motivates **Q2**: if we set aside computational cost, is an exact polar factor always preferable, or can inexact projection qualitatively change discrete-time dynamics in a way that can *help* optimization?

### 3 Exact Projection with Fixed Step Sizes: Grid Confinement, Rates, and What They (Don’t) Explain

This section isolates a single design choice that is often idealized in theory: *exact* Stiefel/polar projection (equivalently, an exact spectral-norm LMO / exact matrix sign), combined with fixed step sizes. Our goal is not to advocate this idealization, but to understand precisely what it implies—and what it fails to imply—already on smooth strongly convex objectives. We ask:

**Q1:** *With exact projection and fixed step sizes, does a MUON-style update necessarily reach the global minimizer of a smooth, strongly convex objective? If it can reach a loss level  $\varepsilon$ , what is the best possible dependence on  $\varepsilon$ ? Besides the dependence on  $\varepsilon$ , what could explain speedups in practice—perhaps through conditioning-dependent constants?*

For reference, the (usually unique) polar factor of a matrix  $M \in \mathbb{R}^{d_1 \times d_2}$  with SVD

$$M = U\Sigma V^\top \quad \text{is} \quad \mathcal{P}(M) = UV^\top, \quad (1)$$

where  $d = \min(d_1, d_2)$ , matrices  $U \in \mathbb{R}^{d_1 \times d}$ ,  $V \in \mathbb{R}^{d_2 \times d}$  have orthonormal columns, and  $\Sigma = \text{diag}(\sigma_1, \dots, \sigma_d)$  holds the singular values  $\sigma_1 \geq \dots \geq \sigma_d \geq 0$ .

#### 3.1 Global convergence to minimizer?

We start with convergence to the global minimizer. We exhibit a simple counterexample where, for generic initializations, the iterates become confined to discrete lattices and miss sufficiently small loss balls, even on simple strongly convex quadratics. We then explain how this is reflected in existing stationarity-type bounds through an irreducible residual term. The only remedy to have a generic convergence result is to let the effective step size vanish.

Consider the isotropic quadratic loss

$$L(W) = \frac{1}{2} \|W\|_F^2, \quad W \in \mathbb{R}^{d \times d}, \quad (2)$$

which is smooth and strongly convex, with  $\nabla L(W) = W$ . The exact Stiefel/polar update (no momentum) with constant step size  $\alpha > 0$  is

$$W_{t+1} = W_t - \alpha \mathcal{P}(W_t). \quad (3)$$

If  $W_0 = US_0V^\top$  with  $U, V$  orthogonal and  $S_0$  diagonal with entries  $s_{0,1}, \dots, s_{0,d}$  (not necessarily non-negative), then  $\mathcal{P}(W_0) = U \text{sign}(S_0)V^\top$ , where  $\text{sign}(S_0)$  is diagonal with entries  $\text{sign}(s_{0,i})$ . Thus,  $W_1 = W_0 - \alpha \mathcal{P}(W_0) = U(S_0 - \alpha \text{sign}(S_0))V^\top$ : the matrices  $U, V$  remain unchanged. By induction,  $W_t = US_tV^\top$  for all  $t$ , with  $S_t = \text{diag}(s_{t,1}, \dots, s_{t,d})$  following simple dynamics ( $d$  separate scalar recursions):

$$s_{t+1,i} = s_{t,i} - \alpha \text{sign}(s_{t,i}). \quad (4)$$

Since  $L(W_t) = \frac{1}{2} \sum_{i=1}^d s_{t,i}^2$ , the overall dynamics reduce to  $d$  independent copies of 1-D sign-GD:

$$\ell(s) = \frac{1}{2}s^2, \quad s_{t+1} = s_t - \alpha \operatorname{sign}(s_t). \quad (5)$$

This trajectory remains on the lattice  $s_0 + \alpha\mathbb{Z}$ . Starting from  $s_0 > 0$ , it decreases by  $\alpha$  until it crosses 0, and then it falls into a 2-cycle between the two lattice points closest to 0. Consequently, unless  $s_0 \in \alpha\mathbb{Z}$  (an unlikely condition under generic initialization), the iterates never reach arbitrarily small neighborhoods of the minimizer. On the matrix quadratic (2), the same grid confinement occurs simultaneously across all singular values via (4), so the obstruction persists, even though the loss is smooth and strongly convex.

**Momentum does not break grid confinement.** There are multiple natural ways to combine momentum with Stiefel/polar steps; we summarize the main variants and their relation to MUON in Section B. MUON’s official implementation computes a momentum term  $m_{t,i}$  *before* projection, and takes a step along the projected momentum:

$$s_{t+1,i} = s_{t,i} - \alpha \operatorname{sign}(m_{t,i}), \quad (6)$$

so  $s_{t,i} \in s_{0,i} + \alpha\mathbb{Z}$  for all  $t$ . Thus, the same lattice obstruction persists. This answers the first part of **Q1** negatively for exact projection with fixed step sizes, with or without MUON-style momentum.

**Implications for worst-case smooth theory: where grid confinement appears in stationarity results.** Despite the negative reachability result above, there are many existing stationarity-type guarantees for MUON that establish convergence to stationary points. We now explain how grid confinement manifests in these results, and how these results implicitly acknowledge the need for vanishing step sizes to converge to stationarity.

For a constant step size  $\alpha$ , simple algebraic manipulations of standard descent-lemma arguments yield

$$\left[ \min_{0 \leq t \leq T-1} \|\nabla L(W_t)\|_* \right] \leq \frac{L(W_0) - L_*}{T\alpha} + \frac{c}{2} d\alpha. \quad (7)$$

It is valid for any  $c$ -smooth loss  $L: \mathbb{R}^{d_1 \times d_2} \rightarrow \mathbb{R}$ , assuming  $T$  steps from initialization  $W_0$ , with exact projection and fixed step size  $\alpha > 0$  (see Section C). Here,  $\|\cdot\|_*$  is the nuclear norm,  $d = \min(d_1, d_2)$ , and  $L_* = \inf_W L(W)$ .

Variants of this type of bound appear as an intermediary step in many (if not all) existing stationarity analyses for MUON Pethick et al. [2025], Li and Hong [2025], Shen et al. [2025], Chen et al. [2025], Kovalev [2025], Riabinin et al. [2025], Gruntkowska et al. [2025], Sato et al. [2025], Shulgin et al. [2025], Kim and Oh [2026], Lau et al. [2025], Nagashima and Iiduka [2026]. As  $T \rightarrow \infty$ , the first term vanishes but the second remains: the best stationarity level one can guarantee is  $O(\alpha)$  unless  $\alpha \rightarrow 0$ . This is the analytic “shadow” of grid confinement: fixed step sizes induce a non-vanishing residual term. On losses also satisfying a PL inequality, this translates into a residual suboptimality gap  $L(W_t) - L_*$  of order  $O(\alpha^2)$ , consistent with what we saw on  $L(W) = \frac{1}{2}\|W\|_F^2$  where the floor loss is  $\Theta(\alpha^2)$ . Because of that, existing analyses typically assume vanishing step sizes in their final statements to eliminate this irreducible term and to obtain a convergence result.

Beyond worst-case smooth theory, Ma et al. [2026] study specific quadratic and quartic losses. By restricting to specific objectives, they obtain tighter convergence rates. Their analysis relies on (approximate) decoupling along singular directions, as in (4). That setting must confront the same discrete-time issue highlighted above, and indeed the analysis adopts vanishing step-size schedules to obtain convergence to the minimizer. Our point here is not to compare assumptions, but to emphasize the structural fact: *with exact projection, non-vanishing step sizes are fundamentally incompatible with generic minimizer reachability*.

### 3.2 Best possible $\varepsilon$ -dependence under fixed steps: no better than $O(1/\sqrt{\varepsilon})$

Suppose we ignore the reachability obstruction (e.g., by assuming a lucky initialization that aligns with the lattice, or by asking only for the fastest possible approach to an  $\varepsilon$ -scale neighborhood before cycling). We now ask the second part of **Q1**: *does MUON have an asymptotically better dependence on  $\varepsilon$  than GD on smooth strongly convex objectives, under exact projection and fixed step sizes?*

Answer: **No**, it is at best  $O(1/\sqrt{\varepsilon})$  on a generic strongly convex quadratic, which is worse than GD’s  $O(\log(1/\varepsilon))$ .

To see that it cannot be better than  $O(1/\sqrt{\varepsilon})$ , consider again the isotropic quadratic (2) and its decoupled singular-value dynamics (4). Each step on  $\ell(s) = \frac{1}{2}s^2$  decreases the magnitude of each singular

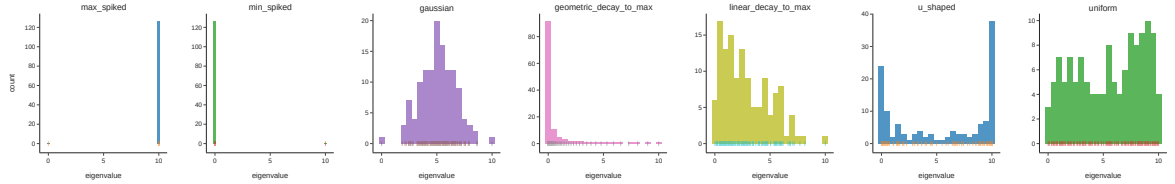


Figure 1: Eigenvalue distributions for the controlled-spectrum families. All families share the same endpoints  $(s_{\min}, s_{\max}) = (10^{-3}, 10)$  and thus the same condition number  $\kappa = s_{\max}/s_{\min} = 10^4$ , but have different spectrum shapes.

value  $s_t$  by exactly  $\alpha$  until the first sign flip where it enters a 2-cycle. Cycling occurs after  $t = \Theta(|s_0|/\alpha)$  steps. The 2-cycle oscillates between values of magnitude at most  $\alpha$ , hence the loss at that point is at most  $\alpha^2/2$ . For the loss to be at most  $\varepsilon$ , we need  $\alpha = O(\sqrt{\varepsilon})$ , resulting in a time-to- $\varepsilon$  loss of  $\Theta(1/\sqrt{\varepsilon})$  steps. This occurs simultaneously across all singular values via (4), so the same scaling applies to the full loss  $L(W) = \frac{1}{2}\|W\|_F^2$ .

**Contrast with GD.** On the same quadratic, GD converges in one step with step size 1. More generally,  $O(1/\varepsilon)$  steps are enough on any smooth *convex* objective, given that the step size is small enough (e.g.,  $1/L$  for  $L$ -smooth functions), and  $O(\log(1/\varepsilon))$  steps suffice under *strong* convexity.

### 3.3 If not $\varepsilon$ -dependence, then what? Conditioning and spectrum shape at a fixed budget

Sections 3.1 and 3.2 rule out a general explanation of MUON’s success based purely on asymptotic  $\varepsilon$ -dependence under exact projection and fixed step sizes. A remaining hypothesis is *finite-budget advantage*: for a fixed iteration budget  $T$ , MUON-style updates might enjoy better problem-dependent constants than GD in the big-O rates.

A common practitioner narrative emphasizes *ill-conditioning* Jordan [2024]: since GD’s worst-case guarantees deteriorate with the condition number  $\kappa$ , while Stiefel/polar updates can achieve rates independent of  $\kappa$  on certain quadratics and quartics Ma et al. [2026], one might expect MUON to systematically outperform GD in poorly conditioned cases.

However, several logical gaps remain. First,  $\kappa$ -insensitivity of MUON in specific worst-case analyses does not imply insensitivity to finer spectral structure at fixed  $\kappa$ . Second, although the worst-case dependence of GD on  $\kappa$  is well understood, average-case analyses indicate that the performance of first-order methods on quadratics generally depends on the *full spectrum* of the Hessian rather than on  $\kappa$  alone Pedregosa and Scieur [2020], Cunha et al. [2022]. What is thus not clear a priori is how sensitive each method is to spectrum shape at fixed  $\kappa$ , and whether these variations are large enough to alter the *relative ordering* between MUON and GD. We therefore turn to the following question:

*Can we construct equally ill-conditioned problems for which the ranking between MUON and GD flips?*

A positive answer would imply that conditioning alone is not predictive of the relative performance of MUON and GD on generic quadratics.

**Experimental setup.** We consider quadratics of the form

$$L(W) = \frac{1}{2}\langle W, AW \rangle + \langle B, W \rangle + c. \quad (8)$$

All matrices are square of size  $n \times n$ , with  $n = 100$ . We set  $A = QSQ^\top$ , with  $Q$  a random orthogonal matrix obtained as the  $Q$  factor of a QR decomposition of a matrix with i.i.d.  $\mathcal{N}(0, 1)$  entries, and  $S = \text{diag}(s_1, \dots, s_n)$  set according to 7 different spectrum shapes (uniform, Gaussian, spiked, etc.; see Figure 1). All spectrum families share the same endpoints  $(s_{\min}, s_{\max})$  and hence the same condition number  $\kappa = s_{\max}/s_{\min}$ . For each quadratic instance, we sample 100 random initializations  $[W_0]_{ij} \stackrel{\text{i.i.d.}}{\sim} \mathcal{N}(0, 1/n)$  and run each optimizer for  $T = 500$  iterations. Learning rates are selected by choosing the run that achieves the smallest loss up to time  $T$ . Full details are given in Section D.

**Main result: at fixed conditioning, MUON can either outperform or underperform GD depending on spectrum shape.** We consider quadratic instances with a large Hessian condition number,  $\kappa = 10^4$ . Across all runs, the gradient condition numbers observed along GD trajectories lie

Table 1: Win rates for exact-projection MUON vs. GD (comparing the best loss achieved by each algorithm across all learning rates, up to time  $t$ ); a “1” means MUON always wins. All spectra share the same endpoints  $(10^{-3}, 10^1)$  and condition number  $\kappa = 10^4$ .

kind	$t = T/10$	$t = T/2$	$t = T$
<code>max_spiked</code>	0	0	0
<code>min_spiked</code>	1	1	1
<code>uniform</code>	0	0	0
<code>gaussian</code>	0	0	0
<code>linear_decay_to_max</code>	0	0	0
<code>u_shaped</code>	0	0	1
<code>geometric_decay_to_max</code>	1	1	1

in a comparable range, between  $10^4$  and  $10^8$  (see Section D.7). Table 1 reports, for each spectrum family, the fraction of initializations for which *exact-projection MUON* (without momentum) achieves a smaller loss than GD at  $t \in \{T/10, T/2, T\}$  over 100 random initializations. The results are binary: for each spectrum shape, MUON either consistently outperforms GD or consistently underperforms it. Since all instances share the same Hessian condition number and include GD runs with similar gradient conditioning (Section D.7), these results show that *conditioning alone does not determine which method is faster* even in this quadratic setting. Despite identical  $\kappa$ , varying only the spectrum shape is sufficient to flip the ranking between MUON and GD. Any general explanation of MUON’s advantage must therefore account for finer spectral structure, or explain why it becomes irrelevant in the regimes of interest.

**Magnitude of loss reduction at fixed  $\kappa$ .** To quantify this effect more directly, we measure how many orders of magnitude each method reduces the loss from the same initialization, averaged over runs. Figure 2 shows that there is at least one order of magnitude difference in loss reduction between MUON and GD in all cases. Moreover, MUON consistently reduces the loss by a similar number of orders of magnitude across all spectrum shapes. In contrast, GD’s reduction varies substantially with the spectrum shape. Thus, at fixed  $\kappa$ , the flip in ranking is primarily driven by the fact that GD’s progress varies substantially with the spectral distribution, while MUON remains comparatively stable across the spectra we test.

**Relation to spectra in neural networks.** We note that the spectrum shapes that favor MUON here, those with a bulk of small eigenvalues and a few large ones (`min_spiked` and `geometric_decay_to_max`), resemble Hessian spectra reported in neural networks Sagun et al. [2017, 2018], Ghorbani et al. [2019], Li et al. [2019], Gur-Ari et al. [2019], Papyan [2020], Song et al. [2025], Tang et al. [2025], though we cannot draw definitive conclusions beyond this qualitative similarity.

**Ablations: vanishing step sizes, other MUON variants, and sample trajectories.** (i) Section D.4 reports the average loss ratios at different steps  $t \in \{T/10, T/2, T\}$ , complementing the final time  $t = T$  results in Figure 2. We also include in Section D.5 the same plot as Figure 2 but including the initial loss level for each spectrum family, instead of just the reduction achieved from it. (ii) Section D.6 shows representative *sample trajectories* per spectrum family to complement the averaged ones in Figure 3. (iii) The same appendix includes ablations with vanishing learning-rate schedules and different MUON variants (with or without Nesterov-style momentum and with exact or Newton–Schulz approximate projection). While vanishing step sizes affect late-stage dynamics, and momentum or approximate projection mainly influence how noisy the loss curves are, they do not change the qualitative conclusion on these quadratics: conditioning alone does not explain MUON’s speed relative to GD. The same ranking across spectra is observed across these variants.

## 4 Approximate Projection Can Change the Dynamics (and Sometimes the Speed)

The previous section analyzed an idealization common in theory: *exact* polar projection with a fixed step size. In practice, however, MUON does *not* compute a polar factor exactly: it applies a low-degree Newton–Schulz-type polynomial (plus implementation choices such as rescaling and momentum). A widespread modeling stance treats this inexactness as a nuisance term that monotonically worsens guarantees relative to the exact baseline. But, is it?

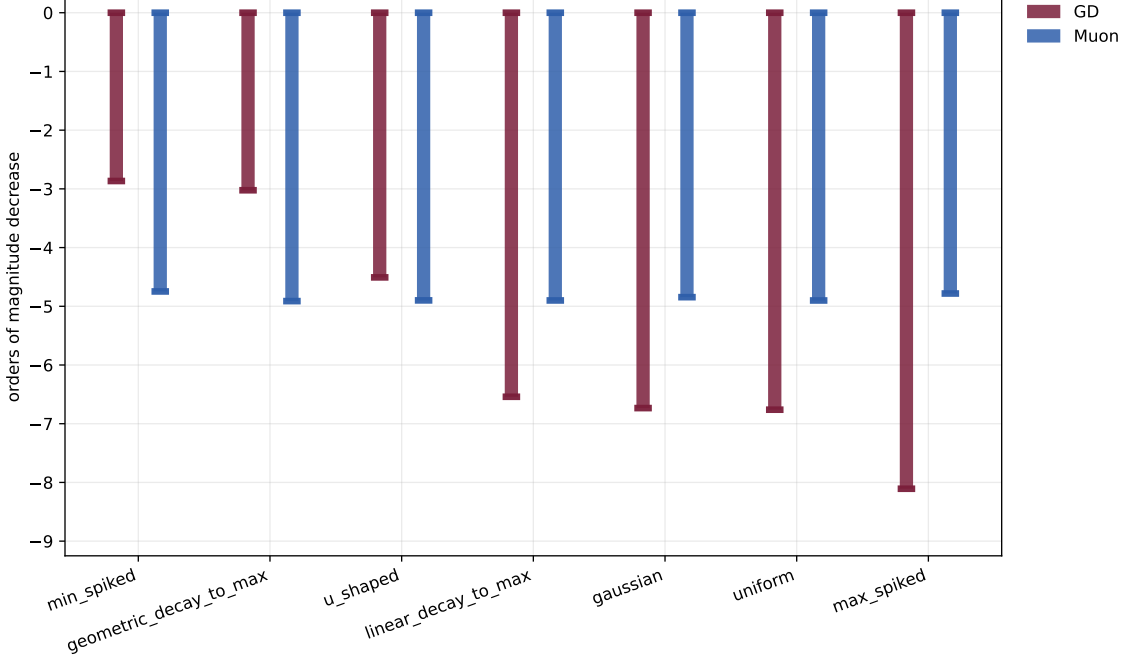


Figure 2: Orders of magnitude of loss decrease after  $T = 500$  iterations on the controlled-spectrum quadratic family (Section 3.3). For each spectrum shape (all sharing the same endpoints and condition number  $\kappa = 10^4$ ), bars are aligned at the common initial loss so that their lengths represent the logarithmic decrease achieved. The vertical axis is indexed by integers  $-1, -2, \dots$ , corresponding to factors of  $10^{-1}, 10^{-2}, \dots$  reduction. MUON achieves a comparable reduction across spectrum families, whereas GD exhibits variation, which shows that the flip in ranking is primarily driven by the fact that the performance of GD depends on the spectral distribution, while MUON remains comparatively stable across the spectra we test. For the `max_spiked` family, GD's loss is numerically very close to 0. For plot readability, we clip the corresponding bar at roughly  $-8$  orders of magnitude.

**Q2:** *Already on simple strongly convex objectives, can approximate projection qualitatively change reachability and change iteration counts?*

#### 4.1 A minimal model: perturbed sign dynamics

On the isotropic quadratic  $L(W) = \frac{1}{2}\|W\|_F^2$ , exact Stiefel updates reduce to coordinate-wise sign dynamics on singular values (Section 3.1). An approximate polar factor replaces each singular value  $s_{t,i}$  by its sign plus a distortion:

$$s_{t+1,i} = s_{t,i} - \alpha(\text{sign}(s_{t,i}) + \eta_{t,i}). \quad (9)$$

In practice, MUON approximates the sign function by one that maps most of  $[0, 1]$  to  $[1 - \delta, 1 + \delta]$ , with  $\delta \approx 0.3$ . This means  $|\eta_{t,i}| \lesssim 0.3$  in practice. These distortions  $\eta_{t,i}$  are neither independent across  $i$  nor across  $t$ . Indeed, all singular values are first jointly mapped to  $[0, 1]$  before applying the polynomial approximation (Code 2). This global rescaling step creates dependencies across  $i$ . Moreover, the optimizer correlates the iterates over time.

Here, we take a first step to analyze and isolate the *role* of inexactness by studying a simplified perturbation model:

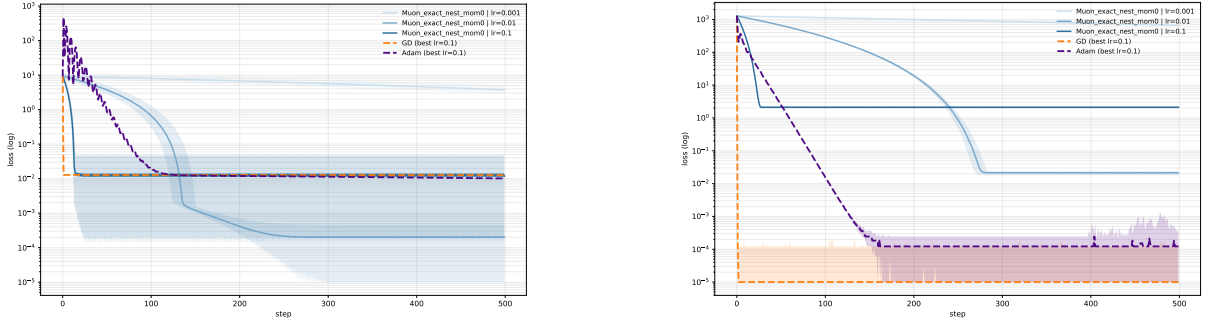
$$s_{t+1} = s_t - \alpha(\text{sign}(s_t) + \sigma \xi_{t+1}), \quad (10)$$

where  $(\xi_t)_t$  are i.i.d. standard Gaussians  $\mathcal{N}(0, 1)$ , and  $\sigma \geq 0$  controls the perturbation magnitude.

#### 4.2 Noise breaks confinement on the isotropic quadratic, and typical hitting times can be non-monotone

Define the hitting time of an  $\varepsilon$ -loss for  $\ell(s) = \frac{1}{2}s^2$  by

$$T_\varepsilon^{(\sigma)} := \inf\{t \geq 0 : \ell(s_t) \leq \varepsilon\},$$



(a) `min_spiked` spectrum (favorable to MUON).

(b) `max_spiked` spectrum (unfavorable to MUON).

Figure 3: Averaged loss curves with shaded bands covering 95% of trajectories for the quadratic objective  $L(W) = \frac{1}{2}\langle W, AW \rangle + \langle B, W \rangle + c$ , averaged over 100 random initializations  $[W_0]_{ij} \stackrel{\text{i.i.d.}}{\sim} \mathcal{N}(0, 1/n)$ . Across panels, the matrix  $A$  has the same condition number but different spectrum shapes (see Figure 1). On the `min_spiked` spectrum, the loss achieved by GD is numerically very close to zero. We clip it at  $10^{-5}$  for plot readability.

where  $(s_t)_{t \geq 0}$  follows (9) with some given  $s_0$ . For  $\sigma = 0$ , the trajectory remains on a lattice  $s_0 + \alpha\mathbb{Z}$  and generically falls into a two-cycle around 0, making sufficiently small loss levels unreachable. A first key observation is that noise breaks this lattice confinement: as soon as  $\sigma > 0$ , reachability is restored almost surely; see Theorem E.1 for a precise statement and Section E.1 for a proof.

Beyond reachability, we consider a practical proxy: the distribution of  $T_\varepsilon^{(\sigma)}$  as a function of  $\sigma$ . On the 1D toy model (10), the typical scale of  $T_\varepsilon^{(\sigma)}$  deteriorates both as  $\sigma \rightarrow 0$  (recovering near-deterministic cycling) and as  $\sigma \rightarrow \infty$  (diffusive overshoot dominates). Indeed, it must be greater than any fixed  $t$  with high probability in both limits:  $\mathbb{P}(T_\varepsilon^{(\sigma)} > t) \rightarrow 1$  as  $\sigma \rightarrow 0$  or  $\sigma \rightarrow \infty$  for any fixed  $t$ ; see Theorem E.2 and Section E.2.

In experiments, we report the typical iteration count needed to reach  $\varepsilon$ -loss (median of  $T_\varepsilon^{(\sigma)}$ ) over  $10^4$  independent runs. For reference, the baseline  $\lceil s_0/\alpha \rceil$  corresponds to the number of steps at which the noiseless trajectory first crosses 0 and enters the cycling phase, and thus represents the fastest possible approach to  $\varepsilon$ -loss *without* noise.

Figure 4 shows that the iteration count is *non-monotone* in  $\sigma$ : there is a “sweet spot”, an intermediate noise level, which improves which losses are reachable in a fixed iteration count. Noise is therefore *beneficial* on this toy model.

### 4.3 Quadratic evidence with actual Newton–Schulz projection: approximation can change who wins

The synthetic perturbation model above isolates a mechanism, but Newton–Schulz approximation is not i.i.d. noise. We therefore also test with the actual Newton–Schulz approximate projection on the same controlled-spectrum quadratic family as in Section 3.3. We compare two MUON variants: MUON with exact projection vs. MUON with Newton–Schulz approximate projection (under no momentum and constant step sizes; details in Section F.2).

Table 2 reports win rates (over random initializations) for MUON with Newton–Schulz approximate projection vs. MUON with exact projection at milestones  $t \in \{T/10, T/2, T\}$ . The outcome is *not uniform across spectra*: in the most favorable shape for MUON in Section 3.3 (min-spiked), the approximate method tends to reach smaller losses by time  $T$ , while on many other shapes it does not.

Section F.2 complements Table 2 with mean best-loss ratios: when approximate projection wins, it does so by a significant margin in best-loss value (e.g.,  $30\times$  smaller), otherwise it remains within a factor 2 of the exact method. Taken together, these experiments support that: *approximate projection can matter for iteration complexity, but whether it helps or not depends on the setup*. This makes it difficult to justify a universal “approximation is worse / better” abstraction, and it motivates more fine-grained theory of inexact polar steps that goes beyond monotone degradation with an error magnitude. In particular, what are the effects of different error profiles (e.g. bounded vs. heavy-tailed, centered vs. biased) Amsel et al. [2025]?

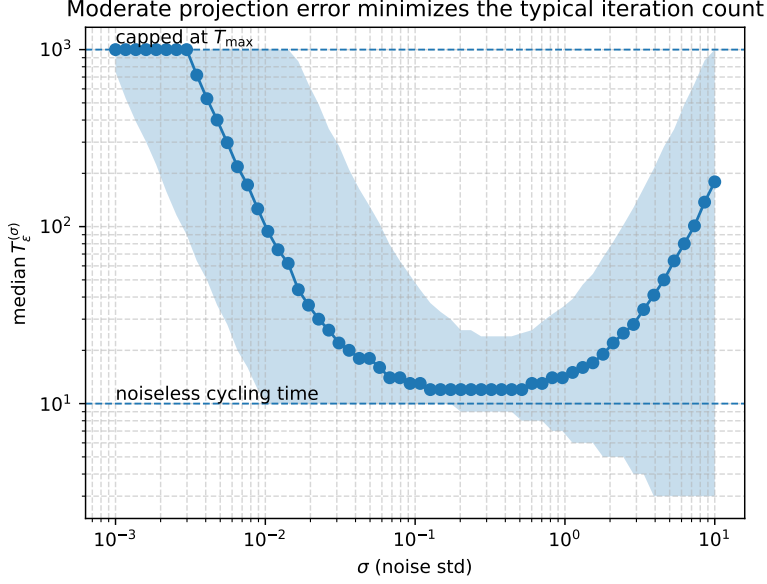


Figure 4: Median  $\varepsilon$ -hitting time exhibits a similar ‘‘sweet spot’’ where moderate projection error  $\sigma$  in (10) accelerates convergence.  $T_\varepsilon^{(\sigma)}$  capped at  $T_{\max} = 1000$  steps (top dashed line). Noiseless cycling time  $|s_0|/\alpha$  shown for reference (bottom dashed line). The shaded band shows the central 95% interval of  $T_\varepsilon^{(\sigma)}$  across runs. Details in Section F.1.

Table 2: Win rates for MUON with Newton–Schulz approximate projection vs. MUON with exact projection, comparing the best loss achieved across learning rates up to time  $t$ . Spectrum naming matches Figure 6; see Section F.2 for exact definitions and hyperparameters.

kind	$t = T/10$	$t = T/2$	$t = T$
max_spiked	0	0	0.92
min_spiked	0.46	0.57	0.94
uniform	0	0	0
gaussian	0	0	0
linear_decay_to_max	0	0	0
u_shaped	0	0	0
geometric_decay_to_max	0	0	0

## 5 One-Step Improvement on Quadratics is Not a Reliable Proxy for End-to-End Speed

A recurring narrative (cf. Q3) is that MUON-like directions are preferable because, on a quadratic or locally quadratic model, they can achieve a larger *per-iteration* decrease than the Euclidean gradient direction when paired with a suitable step size (often motivated by line search on a quadratic proxy) [Davis and Drusvyatskiy \[2025\]](#), [Su \[2025\]](#). This type of argument is appealing because it is local, interpretable, and easy to validate numerically on a single step. Here, we aim at clarifying what local analysis can and cannot certify about full trajectories in general. We observe the following:

*Even on quadratics—the setting most favorable to existing one-step proxy arguments—greedy per-step superiority does not necessarily imply faster end-to-end convergence.*

**Setup.** Consider the quadratic  $L(W) = \frac{1}{2}\langle W, AW \rangle$ . At an iterate  $W$ , we compare two update directions: the Euclidean gradient direction  $D_{\text{GD}}(W) = \nabla L(W)$ , and the Stiefel/polar direction  $D_{\text{St}}(W) = \mathcal{P}(\nabla L(W))$ . To avoid privileging either method through a step-size choice, we let each direction take its own *exact* line-search step size  $\alpha^*(D) \in \arg \min_{\alpha \in \mathbb{R}} L(W - \alpha D)$ . The associated one-step decrease is  $\Delta(D) := L(W) - L(W - \alpha^*(D)D)$ . The local narrative ‘‘Stiefel is better than GD’’ corresponds to regimes where  $\Delta(D_{\text{St}}) > \Delta(D_{\text{GD}})$ .

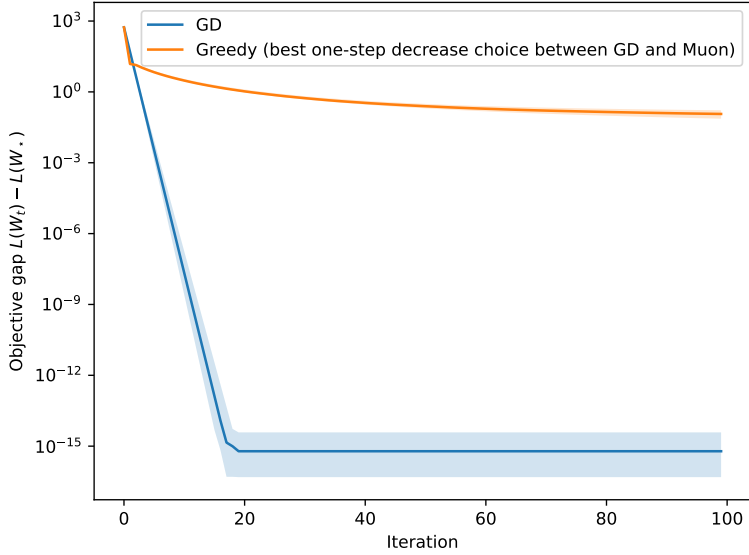


Figure 5: Objective gap  $L(W_t) - L(W_*)$  for the quadratic  $L(W) = \frac{1}{2}\langle W, AW \rangle$  (all matrices are  $n \times n$ ,  $n = 100$ ). Here  $A = QSQ^\top$  with  $Q$  random orthogonal and  $S = \text{diag}(1, \dots, 1, 10^3)$ , so  $\kappa = 10^3$ . We compare GD (exact line search along the Euclidean gradient) to a *greedy* policy that, at each iteration, picks the direction (gradient or Stiefel/polar) yielding the larger exact line-search decrease. On this instance, the greedy policy selects the Stiefel/polar step at every iteration, yet GD converges much faster end-to-end. Curves show the median across 100 random initializations  $W_0$  with i.i.d. entries  $(W_0)_{ij} \sim \mathcal{N}(0, 1/n)$ ; shaded bands contain the central 95% of runs.

**Observation: local advantage can coexist with global disadvantage.** There exist quadratics and initializations  $W_0$  such that a *greedy* policy that, at each iterate, chooses between a gradient step and a Stiefel/polar step, each with its own *optimal* line-search step size, yet has a worse end-to-end loss decrease than GD with line search. Figure 5 illustrates this (and Section G reports how the greedy policy also loses on the gradient norm and distance to the minimizer).

For more general objectives, the message is the same: extra care is needed when one-step comparisons are made via quadratic proxies (e.g., a Taylor expansion or a local quadratic upper bound): we just saw that even on true quadratics, where there is no proxy gap, *one-step superiority does not imply end-to-end speed-up*. This suggests that one-step improvement arguments should come with additional structure that rules out the exhibited phenomena.

## 6 Conclusion

This work highlights that the behavior of MUON is governed by discrete-time phenomena that are not yet fully understood, even on simple strongly convex quadratics.

Addressing these aspects theoretically likely requires new tools: one-step local proxies are generally not sufficient to predict end-to-end speed-up, and worst-case guarantees can yield pessimistic predictions that degrade monotonically with approximation error.

The analysis suggests that at least two ingredients deserve finer modeling: (i) the spectral properties of the loss beyond mere conditioning, affecting big-O constants; and (ii) the approximation error in the polar projection step, which qualitatively alters reachability and can accelerate hitting times. Open questions remain on how best to characterize these aspects theoretically.

## Acknowledgements

This work was supported in part by the Swiss State Secretariat for Education, Research and Innovation (SERI) under contract number MB22.00027.

## References

Kwangjun Ahn, Byron Xu, Natalie Abreu, Ying Fan, Gagik Magakyan, Pratyusha Sharma, Zheng Zhan, and John Langford. Dion: Distributed orthonormalized updates. 2025. URL <https://arxiv.org/abs/2504.05295>.

Noah Amsel, David Persson, Christopher Musco, and Robert Gower. The polar express: Optimal matrix sign methods and their application to the Muon algorithm. *CoRR*, abs/2505.16932, 2025. doi: 10.48550/ARXIV.2505.16932. URL <https://doi.org/10.48550/arXiv.2505.16932>.

Nicolas Boumal and Antoine Gonon. Designing polynomials for Muon’s polar factorization: Focus on quintics, 2025. URL [www.racetothetbottom.xyz/posts/polar-poly/](http://www.racetothetbottom.xyz/posts/polar-poly/). Accessed January 2026.

Franz Louis Cesista, You Jiacheng, and Keller Jordan. Squeezing 1-2% efficiency gains out of Muon by optimizing the Newton-Schulz Coefficients, February 2025. URL <https://leloykun.github.io/ponder/muon-opt-coeffs/>. Accessed January 2026.

Lizhang Chen, Jonathan Li, and Qiang Liu. Muon optimizes under spectral norm constraints. *CoRR*, abs/2506.15054, 2025. doi: 10.48550/ARXIV.2506.15054. URL <https://doi.org/10.48550/arXiv.2506.15054>.

Leonardo Cunha, Gauthier Gidel, Fabian Pedregosa, Damien Scieur, and Courtney Paquette. Only tails matter: Average-case universality and robustness in the convex regime. In *Proceedings of the 39th International Conference on Machine Learning*, volume 162 of *Proceedings of Machine Learning Research*, pages 4474–4491. PMLR, 17–23 Jul 2022. URL <https://proceedings.mlr.press/v162/cunha22a.html>.

Damek Davis and Dmitriy Drusvyatskiy. When do spectral gradient updates help in deep learning? *CoRR*, abs/2512.04299, 2025. doi: 10.48550/ARXIV.2512.04299. URL <https://doi.org/10.48550/arXiv.2512.04299>.

Behrooz Ghorbani, Shankar Krishnan, and Ying Xiao. An investigation into neural net optimization via hessian eigenvalue density. In Kamalika Chaudhuri and Ruslan Salakhutdinov, editors, *Proceedings of the 36th International Conference on Machine Learning*, volume 97 of *Proceedings of Machine Learning Research*, pages 2232–2241. PMLR, 09–15 Jun 2019. URL <https://proceedings.mlr.press/v97/ghorbani19b.html>.

Ekaterina Grishina, Matvey Smirnov, and Maxim V. Rakhuba. Accelerating Newton-Schulz iteration for orthogonalization via Chebyshev-type polynomials. *CoRR*, abs/2506.10935, 2025. doi: 10.48550/ARXIV.2506.10935. URL <https://doi.org/10.48550/arXiv.2506.10935>.

Kaja Gruntkowska, Alexander Gaponov, Zhirayr Tovmasyan, and Peter Richtárik. Error feedback for Muon and friends. *CoRR*, abs/2510.00643, 2025. doi: 10.48550/ARXIV.2510.00643. URL <https://doi.org/10.48550/arXiv.2510.00643>.

Guy Gur-Ari, Daniel A. Roberts, and Ethan Dyer. Gradient descent happens in a tiny subspace, 2019. URL <https://openreview.net/forum?id=ByeTHsAqtX>.

Chuan He, Zhanwang Deng, and Zhaosong Lu. Low-rank orthogonalization for large-scale matrix optimization with applications to foundation model training. *CoRR*, abs/2509.11983, 2025. doi: 10.48550/ARXIV.2509.11983. URL <https://doi.org/10.48550/arXiv.2509.11983>.

Keller Jordan. Muon: An optimizer for the hidden layers in neural networks. <https://kellerjordan.github.io/posts/muon/>, 2024. Accessed January 2026.

Keller Jordan, Jeremy Bernstein, Brendan Rappazzo, @fernbear.bsky.social, Boza Vlado, You Jiacheng, Franz Cesista, Braden Koszarsky, and @Grad62304977. modded-nanogpt: Speedrunning the nanogpt baseline, 2024. URL <https://github.com/KellerJordan/modded-nanogpt>. Accessed January 13th, 2026.

Shucheng Kang, Haoyu Han, Antoine Groudiev, and Heng Yang. Factorization-free orthogonal projection onto the positive semidefinite cone with composite polynomial filtering, 2025. URL <https://arxiv.org/abs/2507.09165>.

Ahmed Khaled, Kaan Ozkara, Tao Yu, Mingyi Hong, and Youngsuk Park. Muonbp: Faster Muon via block-periodic orthogonalization. *CoRR*, abs/2510.16981, 2025. doi: 10.48550/ARXIV.2510.16981. URL <https://doi.org/10.48550/arXiv.2510.16981>.

Gyu Yeol Kim and Min-hwan Oh. Convergence of Muon with Newton–Schulz. In *The Fourteenth International Conference on Learning Representations*, 2026. URL <https://openreview.net/forum?id=1JSfxtLpLm>.

Dmitry Kovalev. Understanding gradient orthogonalization for deep learning via non-euclidean trust-region optimization. *CoRR*, abs/2503.12645, 2025. doi: 10.48550/ARXIV.2503.12645. URL <https://doi.org/10.48550/arXiv.2503.12645>.

Tim Tsz-Kit Lau, Qi Long, and Weijie Su. Polargrad: A class of matrix-gradient optimizers from a unifying preconditioning perspective. *CoRR*, abs/2505.21799, 2025. doi: 10.48550/ARXIV.2505.21799. URL <https://doi.org/10.48550/arXiv.2505.21799>.

Jean-François Le Gall. *Measure Theory, Probability, and Stochastic Processes*, volume 295 of *Graduate Texts in Mathematics*. Springer Cham, 2022. ISBN 978-3-031-14205-5. doi: 10.1007/978-3-031-14205-5. URL <https://link.springer.com/book/10.1007/978-3-031-14205-5>.

Jiaxiang Li and Mingyi Hong. A note on the convergence of Muon, 2025. URL <https://arxiv.org/abs/2502.02900>.

Xinyan Li, Qilong Gu, Yingxue Zhou, Tiancong Chen, and Arindam Banerjee. Hessian based analysis of sgd for deep nets: Dynamics and generalization, 2019. URL <https://arxiv.org/abs/1907.10732>.

Jingyuan Liu, Jianlin Su, Xingcheng Yao, Zhejun Jiang, Guokun Lai, Yulun Du, Yidao Qin, Weixin Xu, Enzhe Lu, Junjie Yan, Yanru Chen, Huabin Zheng, Yibo Liu, Shaowei Liu, Bohong Yin, Weiran He, Han Zhu, Yuzhi Wang, Jianzhou Wang, Mengnan Dong, Zheng Zhang, Yongsheng Kang, Hao Zhang, Xinran Xu, Yutao Zhang, Yuxin Wu, Xinyu Zhou, and Zhilin Yang. Muon is scalable for LLM training. *CoRR*, abs/2502.16982, 2025. doi: 10.48550/ARXIV.2502.16982. URL <https://doi.org/10.48550/arXiv.2502.16982>.

Jianhao Ma, Yu Huang, Yuejie Chi, and Yuxin Chen. Preconditioning benefits of spectral orthogonalization in Muon, 2026. URL <https://arxiv.org/abs/2601.13474>.

Shuntaro Nagashima and Hideaki Iiduka. Improved convergence rates of Muon optimizer for nonconvex optimization, 2026. URL <https://arxiv.org/abs/2601.19400>.

Vardan Papyan. Traces of class/cross-class structure pervade deep learning spectra. *Journal of Machine Learning Research*, 21(252):1–64, 2020. URL <http://jmlr.org/papers/v21/20-933.html>.

Fabian Pedregosa and Damien Scieur. Acceleration through spectral density estimation. In *Proceedings of the 37th International Conference on Machine Learning*, volume 119 of *Proceedings of Machine Learning Research*, pages 7553–7562. PMLR, 13–18 Jul 2020. URL <https://proceedings.mlr.press/v119/pedregosa20a.html>.

Thomas Pethick, Wanyun Xie, Kimon Antonakopoulos, Zhenyu Zhu, Antonio Silveti-Falls, and Volkan Cevher. Training deep learning models with norm-constrained lmos. In *Forty-second International Conference on Machine Learning, ICML 2025, Vancouver, BC, Canada, July 13-19, 2025*. OpenReview.net, 2025. URL <https://openreview.net/forum?id=20qm2IzTy9>.

Artem Riabinin, Egor Shulgin, Kaja Gruntkowska, and Peter Richtárik. Gluon: Making Muon & Scion great again! (bridging theory and practice of LMO-based optimizers for LLMs). *CoRR*, abs/2505.13416, 2025. doi: 10.48550/ARXIV.2505.13416. URL <https://doi.org/10.48550/arXiv.2505.13416>.

Levent Sagun, Léon Bottou, and Yann LeCun. Eigenvalues of the hessian in deep learning: Singularity and beyond, 2017. URL <https://arxiv.org/abs/1611.07476>.

Levent Sagun, Utku Evci, V. Ugur Güney, Yann N. Dauphin, and Léon Bottou. Empirical analysis of the hessian of over-parametrized neural networks. In *6th International Conference on Learning Representations, ICLR 2018, Vancouver, BC, Canada, April 30 - May 3, 2018, Workshop Track Proceedings*. OpenReview.net, 2018. URL [https://openreview.net/forum?id=rJ01\\_M0Lf](https://openreview.net/forum?id=rJ01_M0Lf).

Naoki Sato, Hiroki Naganuma, and Hideaki Iiduka. Convergence bound and critical batch size of Muon optimizer, 2025. URL <https://arxiv.org/abs/2507.01598>.

Ishaan Shah, Anthony M. Polloreno, Karl Stratos, Philip Monk, Adarsh Chaluvaraju, Andrew Hojel, Andrew Ma, Anil Thomas, Ashish Tanwer, Darsh J. Shah, Khoi Nguyen, Kurt Smith, Michael Callahan, Michael Pust, Mohit Parmar, Peter Rushton, Platon Mazarakis, Ritvik Kapila, Saurabh Srivastava, Somanshu Singla, Tim Romanski, Yash Vanjani, and Ashish Vaswani. Practical efficiency of Muon for pretraining. *CoRR*, abs/2505.02222, 2025. doi: 10.48550/ARXIV.2505.02222. URL <https://doi.org/10.48550/arXiv.2505.02222>.

Wei Shen, Ruichuan Huang, Minhui Huang, Cong Shen, and Jiawei Zhang. On the convergence analysis of Muon. *CoRR*, abs/2505.23737, 2025. doi: 10.48550/ARXIV.2505.23737. URL <https://doi.org/10.48550/arXiv.2505.23737>.

Egor Shulgin, Sultan AlRashed, Francesco Orabona, and Peter Richtárik. Beyond the ideal: Analyzing the inexact Muon update. *CoRR*, abs/2510.19933, 2025. doi: 10.48550/ARXIV.2510.19933. URL <https://doi.org/10.48550/arXiv.2510.19933>.

Minhak Song, Kwangjun Ahn, and Chulhee Yun. Does SGD really happen in tiny subspaces? In *The Thirteenth International Conference on Learning Representations*, 2025. URL <https://openreview.net/forum?id=v6iLQBoIJw>.

Weijie Su. Isotropic curvature model for understanding deep learning optimization: Is gradient orthogonalization optimal? *CoRR*, abs/2511.00674, 2025. doi: 10.48550/ARXIV.2511.00674. URL <https://doi.org/10.48550/arXiv.2511.00674>.

Qian-Yuan Tang, Yufei Gu, Yunfeng Cai, Mingming Sun, Ping Li, zhou Xun, and Zeke Xie. Investigating the overlooked hessian structure: From CNNs to LLMs. In *Forty-second International Conference on Machine Learning*, 2025. URL <https://openreview.net/forum?id=o62ZzfCEwZ>.

Mark Tuddenham, Adam Prügel-Bennett, and Jonathan Hare. Orthogonalising gradients to speed up neural network optimisation, 2022. URL <https://arxiv.org/abs/2202.07052>.

## A Muon in the modded-nanoGPT speedrun setup (pseudocode)

We consider the code used in the [nanoGPT speedrun training script](#), as it stays up-to-date with the latest best practices for performance. A simplified (non-distributed) version is presented in [Code 1](#). In the speedrun setup, MUON is applied primarily to 2D weight matrices (e.g., linear layers), while other parameters (e.g., embeddings, biases, and non-matrix tensors) are typically handled by AdamW.

In particular, [Code 1](#) and [Code 2](#) include for reference the global rescaling applied before the Newton–Schulz-like polynomials ([line 162 in the reference code](#)), the “Nesterov-style” momentum variant ([line 705](#)), and the step size and momentum schedules used in the speedrun ([lines 1519](#) and [355](#)).

Listing 1: Muon update as used in the modded-nanoGPT speedrun (simplified, per-matrix view)

```
def muon_step(W, grad_W, v_W, t, S, T, lr0, weight_decay):
    # schedules
    lr_t = lr0 * speedrun_lr(t, S)
    mu_t = speedrun_momentum(t, T)

    # Nesterov-style momentum
    v_W = mu_t * v_W + (1 - mu_t) * grad_W #v_W is the momentum buffer kept across steps
    m = mu_t * v_W + (1 - mu_t) * grad_W

    # approximate polar direction
    u = polar_express(m)

    # rectangular correction factor used in the speedrun
    s = sqrt(max(1, W.shape[0] / W.shape[1]))

    # parameter update
    W = W - lr_t * s * u

    # weight decay (simplified, implemented in code via gated / cautious decay)
    W = W - lr_t * weight_decay * W

    return W, v_W
```

Listing 2: Speedrun schedules and Polar Express orthogonalization

```
def speedrun_lr(step, S, cooldown_frac=0.55):
    x = step / S
    cooldown_weight = max(0.0, min(1.0, (1 - x) / cooldown_frac))
    lr_min = 0.1
    lr_max = 1.0 + 0.52*(x > 1/3) + 0.21*(x > 2/3)
    return lr_min + cooldown_weight*(lr_max - lr_min)

def speedrun_momentum(step, T, warmup=300, cooldown=50):
    warmup_frac = max(0.0, min(1.0, step / warmup))
    cooldown_frac = max(0.0, min(1.0, (T - cooldown - step) / cooldown))
    momentum_min = 0.85
    momentum_max = 0.95
    return momentum_min + min(warmup_frac, cooldown_frac) * (momentum_max - momentum_min)

polar_express_coeffs = [
    (8.156554524902461, -22.48329292557795, 15.878769915207462),
    (4.042929935166739, -2.808917465908714, 0.5000178451051316),
    (3.8916678022926607, -2.772484153217685, 0.5060648178503393),
    (3.285753657755655, -2.3681294933425376, 0.46449024233003106),
    (2.3465413258596377, -1.7097828382687081, 0.42323551169305323)
]

def polar_express(G):
    """
    Polar Express approximate orthogonalization (5 iterations, bf16).
    """
    pass
```

```

X = G.to(bfloat16)
if X.shape[0] > X.shape[1]:
    X = X.T

X = X / (1.02 * norm(X) + 1e-6)

for (a, b, c) in polar_express_coeffs:
    # compute pol(X) = a * X + b * (X*X^T) * X + c * (X*X^T)^2 * X
    A = X @ X.T
    B = b * A + c * (A @ A)
    X = a * X + B @ X

if G.shape[0] > G.shape[1]:
    X = X.T
return X

```

## B Momentum variants for MUON-like methods

We mention three basic variants of momentum below and clarify their relation with the original MUON implementation (Code 1). We discuss the implications of each variant for the scalar loss  $\ell(s) = \frac{1}{2}s^2$  studied in (5):

Does momentum help escape the lattice confinement  $s_t \in s_0 + \eta\mathbb{Z}$  induced by exact polar projection and constant step size?

Answer: **no**. In the scalar proxy, grid confinement persists for the two MUON-style variants where momentum is applied *before* projection: variants (ii) and (iii) below, the latter being the default in MUON.

While stated in terms of the scalar loss  $\ell(s) = \frac{1}{2}s^2$  for simplicity, with projection  $\mathcal{P}(s) = \text{sign}(s)$ , all three variants extend verbatim to the matrix case by interpreting  $s$  as a matrix, and  $\mathcal{P}(\cdot)$  as the exact polar projection operator.

**(i) Momentum *after* projection (Orthogonal-SGDM).** A first option is to first project, and accumulate momentum on the projected direction (called “Orthogonal-SGDM” in [Tuddenham et al. \[2022\]](#)):

$$m_t = \mu m_{t-1} + (1 - \mu) \mathcal{P}(s_t), \quad s_{t+1} = s_t - \eta m_t. \quad (11)$$

In 1D, this variant does *not* confine every iterate  $s_t$  to the lattice  $s_0 + \eta\mathbb{Z}$ . As explained by [Jordan \[2024\]](#), this variant is however *not* the one used in MUON, since [Tuddenham et al. \[2022\]](#) found it can underperform a well-tuned SGD-momentum baseline.

**(ii) Momentum *before* projection (Muon with standard SGD momentum).** This is SGD with classical momentum, with the polar projection applied to the momentum buffer:

$$g_t = \nabla_s \ell(s_t), \quad m_t = \mu m_{t-1} + (1 - \mu) g_t, \quad s_{t+1} = s_t - \eta \mathcal{P}(m_t). \quad (12)$$

In the 1D case  $\ell(s) = \frac{1}{2}s^2$ ,  $\mathcal{P}(m_t) = \text{sign}(m_t) \in \{\pm 1\}$ , so the update step is always  $\pm \eta$ . Hence

$$s_{t+1} - s_t \in \eta\mathbb{Z} \implies s_t \in s_0 + \eta\mathbb{Z} \text{ for all } t, \quad (13)$$

and the lattice obstruction from the no-momentum case remains. This variant is discussed in [Jordan \[2024\]](#), but not the default choice in MUON.

**(iii) Nesterov-style momentum *before* projection (Muon default).** This is the default choice in MUON (Code 1). It applies a Nesterov-style momentum before projection:

$$\begin{aligned} g_t &= \nabla_s \ell(s_t) \\ m_t &= \mu m_{t-1} + (1 - \mu) g_t \\ \tilde{m}_t &= \mu m_t + (1 - \mu) g_t \\ s_{t+1} &= s_t - \eta \mathcal{P}(\tilde{m}_t). \end{aligned} \quad (14)$$

Again, in the scalar proxy we have  $\mathcal{P}(\tilde{m}_t) = \text{sign}(\tilde{m}_t) \in \{\pm 1\}$ , so  $s_{t+1} - s_t \in \{\pm \eta\}$  and therefore  $s_t \in s_0 + \eta\mathbb{Z}$  for all  $t$ . Thus the same grid confinement mechanism persists.

## C Simple Stationarity Result

A standard descent-lemma argument (used throughout the MUON stationarity literature) yields the following generic inequality, which is Equation (7) in the main text, with  $d = \min(d_1, d_2)$ :

$$\left[ \min_{0 \leq t \leq T-1} \|\nabla L(W_t)\|_* \right] \leq \frac{L(W_0) - L_*}{T\alpha} + \frac{c}{2} d \alpha. \quad (15)$$

Assume  $L: \mathbb{R}^{d_1 \times d_2} \rightarrow \mathbb{R}$  is  $c$ -smooth w.r.t. the Frobenius norm, i.e.,

$$L(W') \leq L(W) + \langle \nabla L(W), W' - W \rangle + \frac{c}{2} \|W' - W\|_F^2 \quad \forall W, W' \in \mathbb{R}^{d_1 \times d_2}.$$

Consider the exact Stiefel / polar / spectral-norm LMO update (1) with step sizes  $\alpha_t > 0$ :

$$W_{t+1} = W_t - \alpha_t U_t V_t^\top, \quad \nabla L(W_t) = U_t \text{diag}(\sigma_{t,1}, \dots, \sigma_{t,d}) V_t^\top, \quad (16)$$

where  $U_t \in \mathbb{R}^{d_1 \times d}$  and  $V_t \in \mathbb{R}^{d_2 \times d}$  have orthonormal columns and  $\sigma_{t,i} \geq 0$  are the singular values of the gradient at  $W_t$ .

Aiming to plug  $W' = W_{t+1}$  and  $W = W_t$  in the inequality above, notice  $W' - W = -\alpha_t U_t V_t^\top$ ,  $\|U_t V_t^\top\|_F^2 = d$  and  $\langle \nabla L(W_t), U_t V_t^\top \rangle = \sum_i \sigma_{t,i} = \|\nabla L(W_t)\|_*$ . Then, the inequality gives

$$L(W_{t+1}) \leq L(W_t) - \alpha_t \|\nabla L(W_t)\|_* + \frac{c}{2} d \alpha_t^2. \quad (17)$$

Rearrange and sum for  $t = 0, \dots, T-1$ :

$$\sum_{t=0}^{T-1} \alpha_t \|\nabla L(W_t)\|_* \leq L(W_0) - L(W_T) + \frac{c}{2} d \sum_{t=0}^{T-1} \alpha_t^2 \leq L(W_0) - L_* + \frac{c}{2} d \sum_{t=0}^{T-1} \alpha_t^2,$$

where  $L_* := \inf_W L(W)$ . Since  $\alpha_t > 0$  for all  $t$ , we find

$$\min_{0 \leq t \leq T-1} \|\nabla L(W_t)\|_* \leq \frac{L(W_0) - L_*}{\sum_{t=0}^{T-1} \alpha_t} + \frac{c}{2} d \frac{\sum_{t=0}^{T-1} \alpha_t^2}{\sum_{t=0}^{T-1} \alpha_t}.$$

Taking  $\alpha_t = \alpha$  constant gives (15).

## D Controlled-spectrum quadratic experiments

### D.1 Problem family and spectrum shapes

All quadratic objectives in Section 3.3 are derived from a noiseless linear least-squares problem. We consider matrix parameters  $W \in \mathbb{R}^{d_{\text{in}} \times d_{\text{out}}}$  and define

$$L(W) = \frac{1}{2n d_{\text{out}}} \|XW - Y\|_F^2, \quad (18)$$

where  $X \in \mathbb{R}^{n \times d_{\text{in}}}$  and  $Y \in \mathbb{R}^{n \times d_{\text{out}}}$ . Expanding (18) yields the expression

$$L(W) = \frac{1}{2} \langle W, AW \rangle + \langle B, W \rangle + c, \quad A = \frac{1}{n d_{\text{out}}} X^\top X, \quad B = -\frac{1}{n d_{\text{out}}} X^\top Y, \quad c = \frac{1}{2n d_{\text{out}}} \|Y\|_F^2.$$

**Construction of  $X$  with prescribed spectrum.** We set  $n = d_{\text{in}} = d_{\text{out}} = 100$ . To control the spectrum of  $A$ , we construct  $X$  directly from a prescribed eigenvalue sequence. For a chosen spectrum family and fixed  $s_{\max} > s_{\min} > 0$ , we generate then sort eigenvalues  $s_1 \geq \dots \geq s_n \in [s_{\min}, s_{\max}]$  while enforcing the endpoints  $s_1 = s_{\max}$  and  $s_n = s_{\min}$ . We then define singular values

$$\sigma_i = \sqrt{n d_{\text{out}} s_i}, \quad i = 1, \dots, n,$$

and construct

$$X = U \text{diag}(\sigma) V^\top,$$

where  $U \in \mathbb{R}^{n \times n}$  and  $V \in \mathbb{R}^{n \times n}$  are random orthogonal matrices obtained as the  $Q$  factors of QR factorizations computed by `torch.linalg.qr` applied to matrices with i.i.d.  $\mathcal{N}(0, 1)$  entries. By construction,

$$A = \frac{1}{n d_{\text{out}}} X^\top X = V \text{diag}(s) V^\top,$$

so the spectrum of  $A$  is exactly  $\{s_i\}$ .

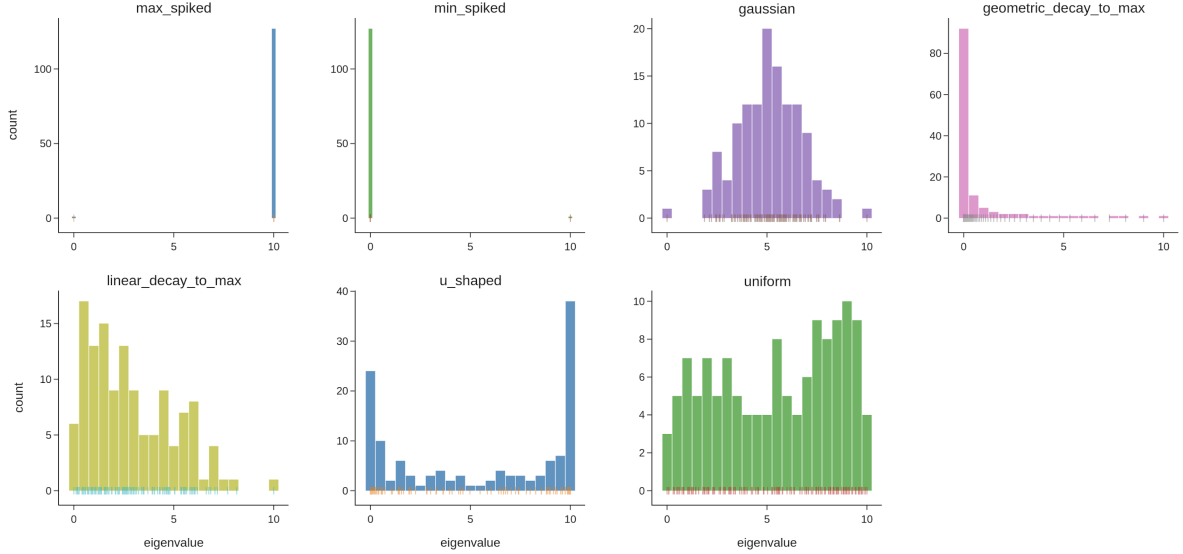


Figure 6: Eigenvalue distributions for the controlled-spectrum families used in Section D. All families share the same endpoints  $(s_{\min}, s_{\max}) = (10^{-3}, 10^1)$  and thus the same condition number  $\kappa = s_{\max}/s_{\min} = 10^4$ , but have different spectrum shapes.

**Targets and optimum.** We fix a planted ground-truth matrix  $W_*$  and set  $Y = XW_*$ . The problem is noiseless, and since  $s_{\min} > 0$ , the minimizer is unique and given by  $W_*$ , with  $L(W_*) = 0$  up to numerical precision.

**Spectrum families.** Across all experiments we fix  $s_{\min} = 10^{-3}$  and  $s_{\max} = 10$ , so that the condition number is  $\kappa = 10^4$ . We vary only the *shape* of the spectrum (Figure 6):

- **max\_spiked:**  $s_n = s_{\min}$  and  $s_1 = \dots = s_{n-1} = s_{\max}$  (a single small eigenvalue, mass at the top).
- **min\_spiked:**  $s_1 = s_{\max}$  and  $s_2 = \dots = s_n = s_{\min}$  (a single large eigenvalue, mass at the bottom).
- **uniform:** eigenvalues sampled i.i.d. uniformly in  $[s_{\min}, s_{\max}]$ , then sorted and endpoints enforced.
- **gaussian:** eigenvalues sampled i.i.d. from a truncated normal distribution centered at  $(s_{\min} + s_{\max})/2$ . For  $k := 3$ ,  $\text{mid} := (s_{\min} + s_{\max})/2$ , and  $\sigma := (s_{\max} - s_{\min})/(2k)$ , we sample  $z_i \sim \mathcal{N}(0, 1)$  i.i.d., clip to  $[-k, k]$ , set  $\tilde{s}_i = \text{mid} + \sigma z_i$ , then sort and enforce endpoints.
- **linear\_decay\_to\_max:** eigenvalues sampled (then sorted) via  $\tilde{s} = s_{\max} - (s_{\max} - s_{\min})\sqrt{u}$  with  $u \sim \text{Unif}[0, 1]$ , yielding higher density near  $s_{\min}$ .
- **geometric\_decay\_to\_max:** a deterministic geometric progression starting at  $s_{\max}$  with ratio  $q = 0.9$ , clipped below at  $s_{\min}$ :  $s_i := \max(s_{\min}, s_{\max} \cdot q^{i-1})$  for  $i = 1, \dots, n$ .
- **u\_shaped:** mixture with mass near both endpoints. We use a symmetric Beta( $\alpha, \alpha$ ) distribution on  $[0, 1]$  with  $\alpha = 0.2$ , mapped affinely to  $[s_{\min}, s_{\max}]$ :  $\tilde{s}_i = s_{\min} + (s_{\max} - s_{\min})z_i$  where  $z_i \sim \text{Beta}(0.2, 0.2)$ .

## D.2 Initialization, horizon, learning-rate selection, and metrics

For each fixed quadratic, we sample 100 i.i.d. initializations  $[W_0]_{ij} \stackrel{\text{i.i.d.}}{\sim} \mathcal{N}(0, 1/n)$ . We run each method for  $T = 500$  iterations.

Learning rates are selected from  $\{10^{-1}, 10^{-2}, 10^{-3}\}$ . When reporting a comparison between two methods, we select, for each method separately, the learning rate that achieves the smallest loss *up to time*  $T$ . This mirrors a finite-budget “best-tuned constant step size” perspective.

We also experiment with vanishing step sizes, using the `torch.optim.lr_scheduler.CosineAnnealingLR` schedule from PyTorch with initial learning rate in  $\{10^{-1}, 10^{-2}, 10^{-3}\}$  and final learning rate  $10^{-3}$  at time  $T$ .

We report: (i) **win rates** (fraction of initializations where optimizer 1 attains lower loss than optimizer 2 at time  $t$ ), and (ii) **magnitude summaries** via mean best-loss ratios, defined as

$$R_t := \frac{\min_{s \leq t} L_s^{\text{optimizer 2}}}{\min_{s \leq t} L_s^{\text{optimizer 1}}},$$

reported as  $\text{mean}(R_t) \pm 1.96$  standard error over initializations.

### D.3 Methods compared

In addition to standard GD and Adam, we study several MUON variants: with or without Nesterov-Style momentum, and with exact or Newton-Schulz approximate projection (turning on or off the relevant features in Code 2).

### D.4 Additional tables: magnitude of improvements

Table 3 reports mean loss ratios, complementing the win-rate in Table 1. This distinguishes “barely wins” from “wins by a large margin” at different milestones  $t = T/10$ ,  $t = T/2$ , and  $t = T$ , instead of just  $t = T$  as in the bar visualizations in Section D.5. We observe that when MUON either wins or loses against GD, it often does so by at least an order of magnitude in loss value.

Table 3: Mean  $\pm 1.96$  standard error (over initializations) of best-GD-loss divided by best-MUON-loss (exact projection, no momentum, constant step size). Values  $> 1$  favor MUON. This can be read as “MUON is better by a factor of **value** on average”.

kind	$t = T/10$	$t = T/2$	$t = T$
<code>max_spiked</code>	$0.00 \pm 0.000000$	$0.00 \pm 0.000000$	$0.00 \pm 0.000000$
<code>min_spiked</code>	$15.0 \pm 6.0$	$165.0 \pm 28.0$	$949.0 \pm 620.0$
<code>uniform</code>	$0.10 \pm 0.0010$	$0.00 \pm 0.000064$	$0.01 \pm 0.00040$
<code>gaussian</code>	$0.00 \pm 0.000003$	$0.00 \pm 0.000007$	$0.00 \pm 0.0005$
<code>linear_decay_to_max</code>	$0.45 \pm 0.0030$	$0.00 \pm 0.000020$	$0.02 \pm 0.0007$
<code>u_shaped</code>	$0.44 \pm 0.003$	$0.11 \pm 0.003$	$2.48 \pm 0.018$
<code>geometric_decay_to_max</code>	$7.0 \pm 0.03$	$10.0 \pm 0.3$	$78.0 \pm 0.3$

### D.5 Bar visualizations: aligned vs. absolute loss levels

To complement the win rates and loss ratios, we report bar plots summarizing final loss levels after  $T = 500$  iterations, averaged over random initializations. We use two visualizations, see Figure 2 and Figure 7 for constant learning rates, and Figure 8 and Figure 9 for vanishing learning rates (same qualitative pattern as in the constant step size setting). The *aligned* version shifts all bars to share a common starting height (the average initial loss are aligned across spectrum families), so that bar length directly represents the number of orders of magnitude by which the loss is reduced. The *not-aligned* version plots the average initial and final loss levels on the same log scale, making absolute starting and ending values visible. These views are complementary: the aligned plot isolates *relative decrease*, while the not-aligned plot reveals the corresponding *absolute scale*. For numerical readability, for the `max_spiked` family we stopped optimizing GD once the loss reached  $10^{-5}$ , even if it keeps improving beyond that point, since the loss has already decreased by at least 8 orders of magnitude and further improvements would distort the scale of the plot and make it harder to visually compare the other spectrum families.

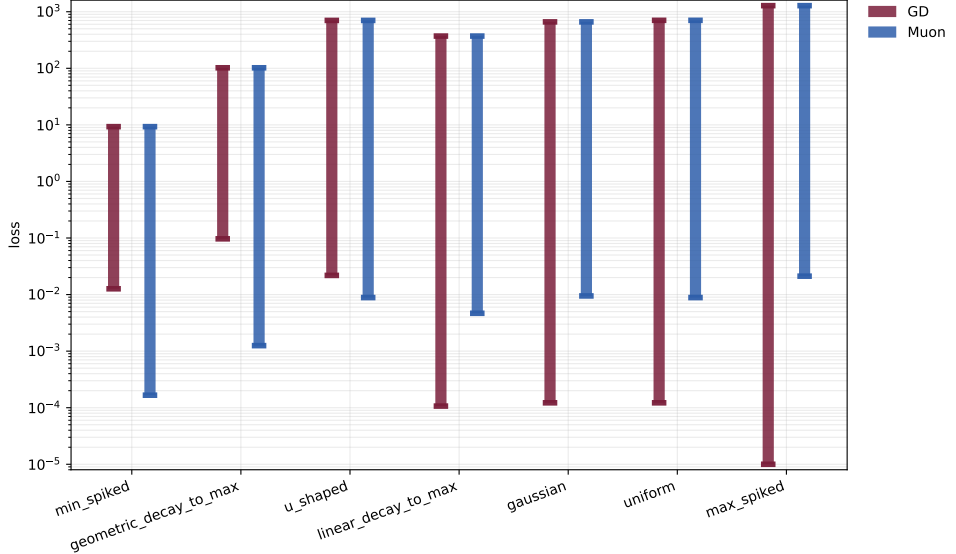


Figure 7: Bar plot of *absolute* initial and final loss levels after  $T = 500$  iterations on the controlled-spectrum quadratic family (constant step size; same setting as Section 3.3). Unlike the aligned view in Figure 2, bars are not shifted and therefore reflect both the starting loss scale and the final loss achieved. For numerical readability, for the `max_spiked` family we clip GD losses below  $10^{-5}$  when plotting. Spectrum families are ordered from left to right by increasing loss reduction achieved by GD relative to its starting loss (while MUON achieves a comparable order-of-magnitude decrease across families).

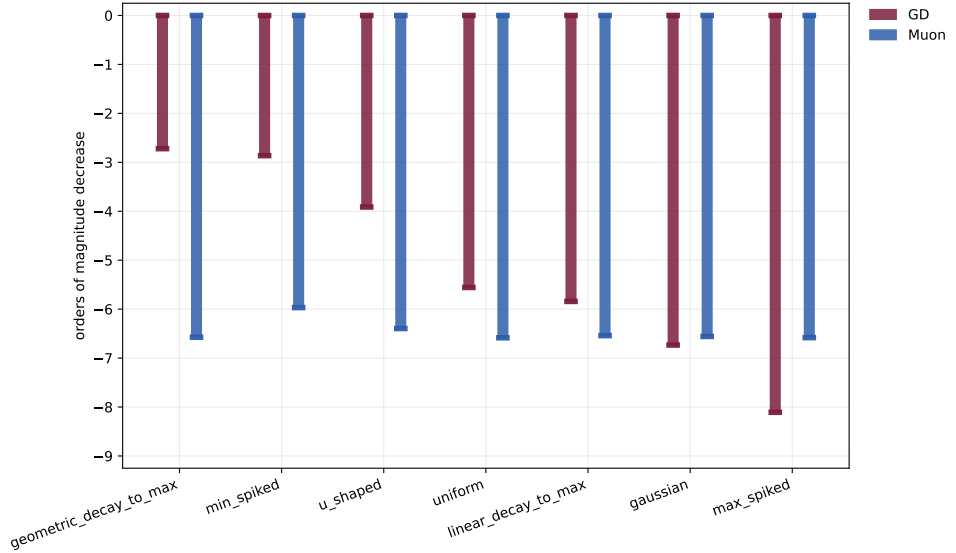


Figure 8: Orders of magnitude of loss decrease after  $T = 500$  iterations under a vanishing learning-rate schedule (CosineAnnealingLR; see Section D.2). Bars are aligned at the common initial loss so that their lengths represent the logarithmic decrease achieved. The same qualitative pattern as in the constant-step setting persists across spectrum families. For numerical readability, for the `max_spiked` family we clip GD losses once they reach  $10^{-5}$  when plotting. Spectrum families are ordered from left to right by increasing loss reduction achieved by GD relative to its starting loss (while MUON achieves a comparable order-of-magnitude decrease across families).

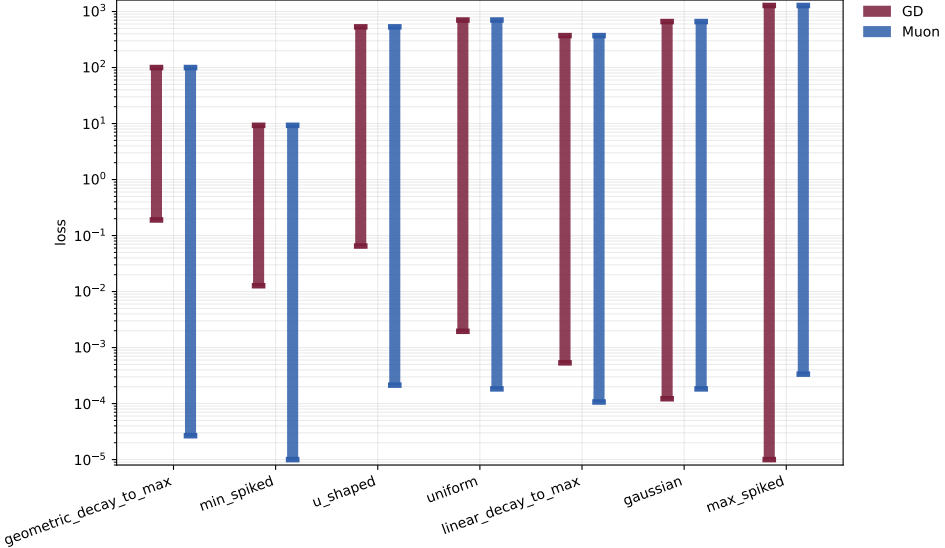


Figure 9: Bar plot of absolute initial and final loss levels after  $T = 500$  iterations under a vanishing learning-rate schedule (same setting as Figure 8). Bars are not shifted and therefore reflect both the starting loss scale and the final loss achieved. For numerical readability, for the `max_spiked` family we clip GD losses below  $10^{-5}$  when plotting. Spectrum families are ordered from left to right by increasing loss reduction achieved by GD relative to its starting loss (while MUON achieves a comparable order-of-magnitude decrease across families).

## D.6 Sample trajectories and robustness checks

We report representative sample trajectories (one random initialization  $W_0$ ) for each spectrum family under two settings: (i) constant-step optimizers with multiple MUON variants (with or without Nesterov-style momentum and with exact or Newton–Schulz approximate projection), and (ii) vanishing step sizes. See Figures 10–13 for representative trajectories across spectrum shapes, shown as paired panels (constant LR vs. vanishing LR) for the same underlying quadratic instance.

These representative trajectories support the qualitative picture of Section 3.3. Across spectrum families, the relative ordering between GD and MUON variants is stable under standard ablations of MUON’s components (momentum and approximate projection). Using vanishing learning-rate schedules primarily affects late-stage dynamics by eventually breaking grid confinement for MUON. However, this typically occurs after GD has already converged, and it does not reverse the relative performance within the fixed iteration budget considered here. Tables 4 to 7 compare GD (best across constant learning rate schedules) to several MUON variants with vanishing learning rates, starting from the exact-projection, no-momentum baseline and successively turning on Newton–Schulz approximation and momentum. Across spectrum families, the dominant ranking between GD and MUON is preserved: spectrum shapes that favor (resp. disfavor) MUON under constant step sizes remain favorable (resp. unfavorable) under these ablations, with only minor quantitative changes in win rates. The same pattern holds when comparing variants of MUON with *constant* step sizes, against GD (not shown here for brevity). Overall, these results reinforce the conclusion that conditioning alone does not explain the relative performance of GD and MUON variants on these quadratics, and that finer spectral structure plays a decisive role.

Table 4: Win rates for MUON (exact projection, no momentum, **vanishing learning rate**) vs. GD, comparing the best loss achieved up to time  $t$ . All spectra share the same endpoints  $(s_{\min}, s_{\max})$  and condition number  $\kappa$ .

kind	$t = T/10$	$t = T/2$	$t = T$
<code>max_spiked</code>	0	0	0
<code>min_spiked</code>	1	1	1
<code>uniform</code>	0	0	0
<code>gaussian</code>	0	0	0
<code>linear_decay_to_max</code>	0	0	0.05
<code>u_shaped</code>	0	0	1
<code>geometric_decay_to_max</code>	1	1	1

Table 5: Win rates for MUON (exact projection **with momentum, vanishing learning rate**) vs. GD, comparing the best loss achieved up to time  $t$ .

kind	$t = T/10$	$t = T/2$	$t = T$
<code>max_spiked</code>	0	0	0
<code>min_spiked</code>	1	1	1
<code>uniform</code>	0	0	0
<code>gaussian</code>	0	0	0
<code>linear_decay_to_max</code>	0	0	0.03
<code>u_shaped</code>	0	0	1
<code>geometric_decay_to_max</code>	1	1	1

Table 6: Win rates for MUON (**Newton–Schulz projection**, no momentum, **vanishing learning rate**) vs. GD, comparing the best loss achieved up to time  $t$ .

kind	$t = T/10$	$t = T/2$	$t = T$
<code>max_spiked</code>	0	0	0
<code>min_spiked</code>	1	1	1
<code>uniform</code>	0	0	0
<code>gaussian</code>	0	0	0
<code>linear_decay_to_max</code>	0	0	0
<code>u_shaped</code>	0	0	1
<code>geometric_decay_to_max</code>	1	1	1

Table 7: Win rates for MUON (**Newton–Schulz projection with momentum, vanishing learning rate**) vs. GD, comparing the best loss achieved up to time  $t$ .

kind	$t = T/10$	$t = T/2$	$t = T$
<code>max_spiked</code>	0	0	0
<code>min_spiked</code>	1	1	1
<code>uniform</code>	0	0	0
<code>gaussian</code>	0	0	0
<code>linear_decay_to_max</code>	0	0	0.31
<code>u_shaped</code>	0	0	1
<code>geometric_decay_to_max</code>	1	1	1

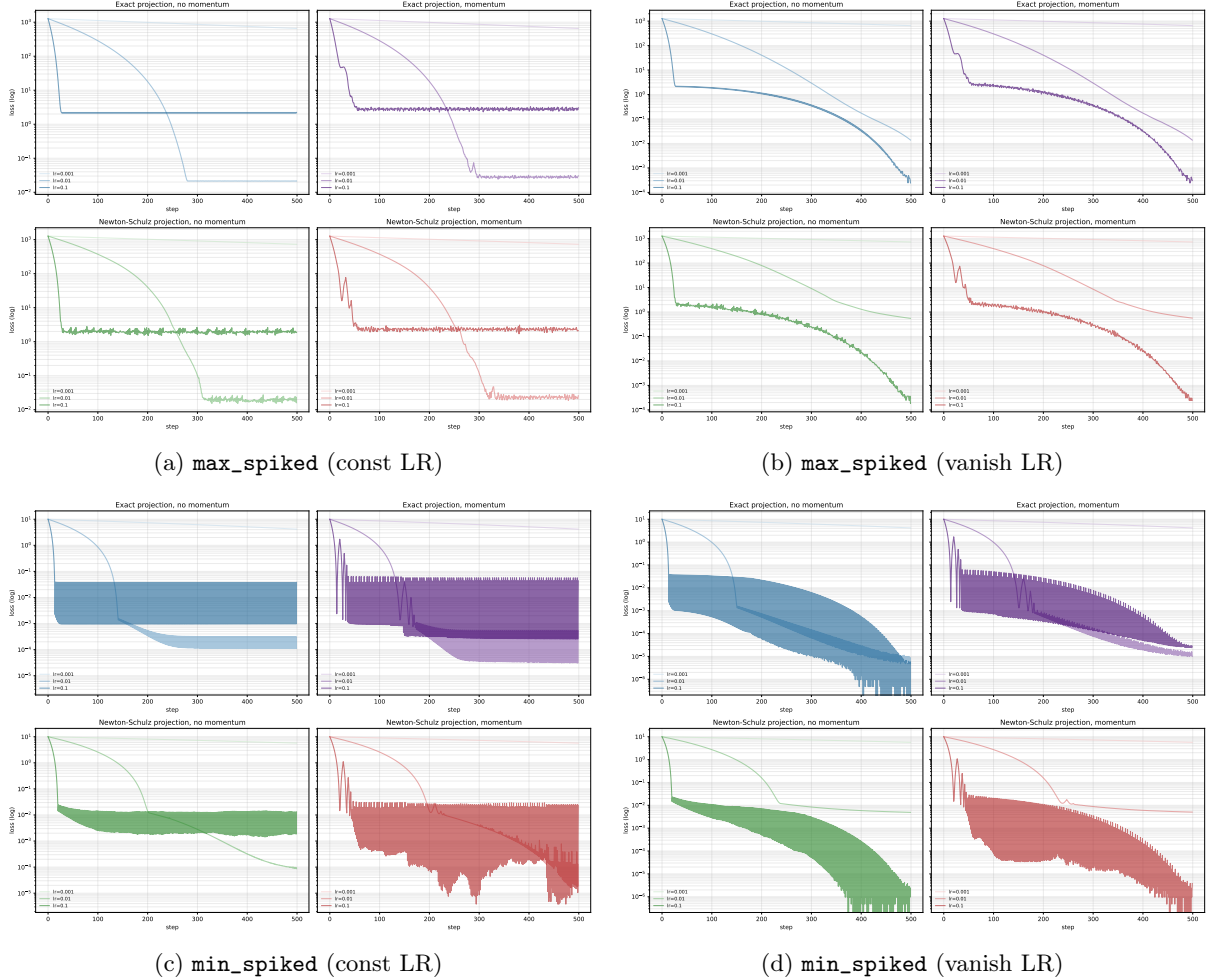


Figure 10: Sample trajectories (one random  $W_0$ ) comparing MUON variants. Left: constant learning rate (LR). Right: vanishing LR.

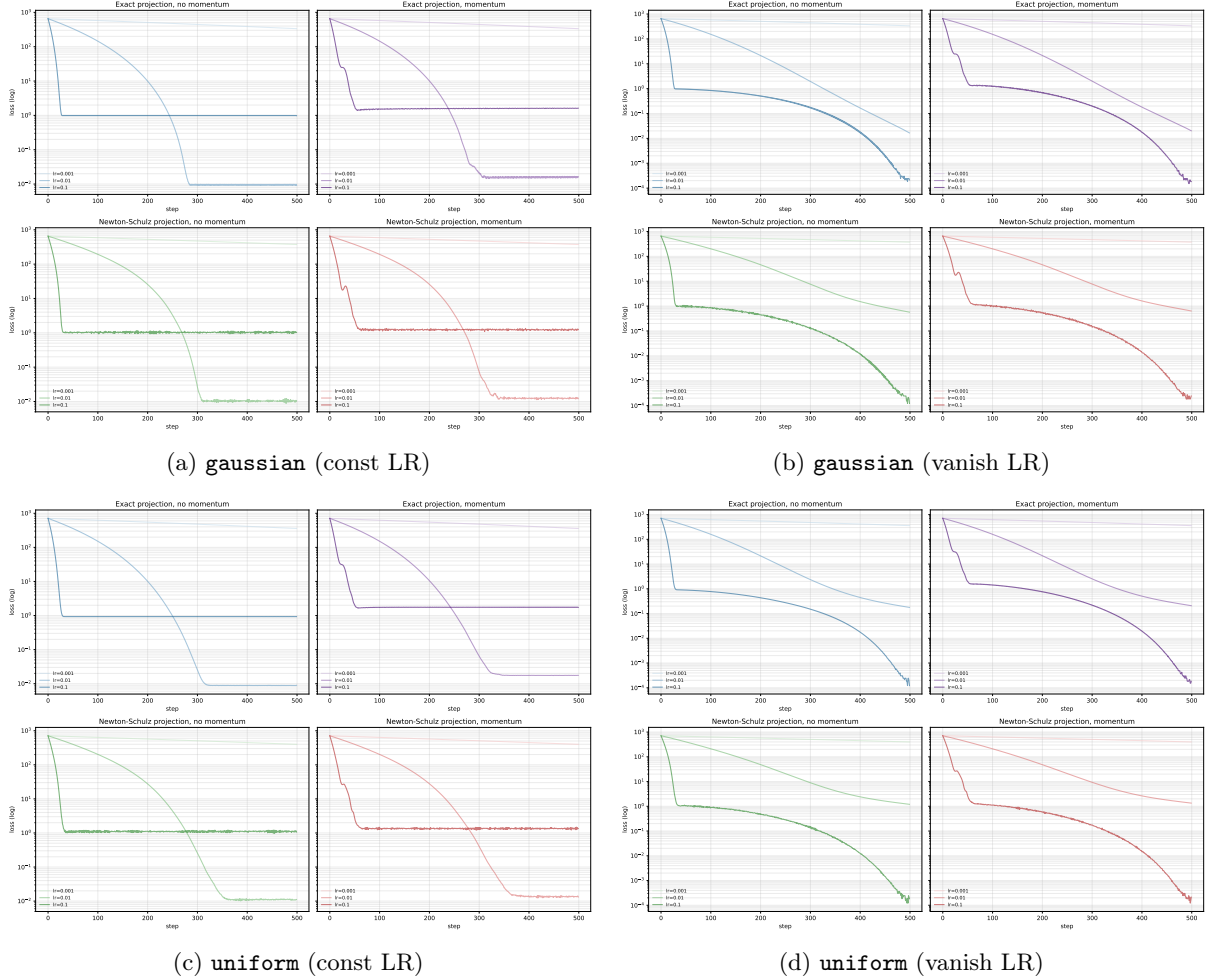


Figure 11: Sample trajectories for **gaussian** and **uniform** spectra (same setting as Figure 10).

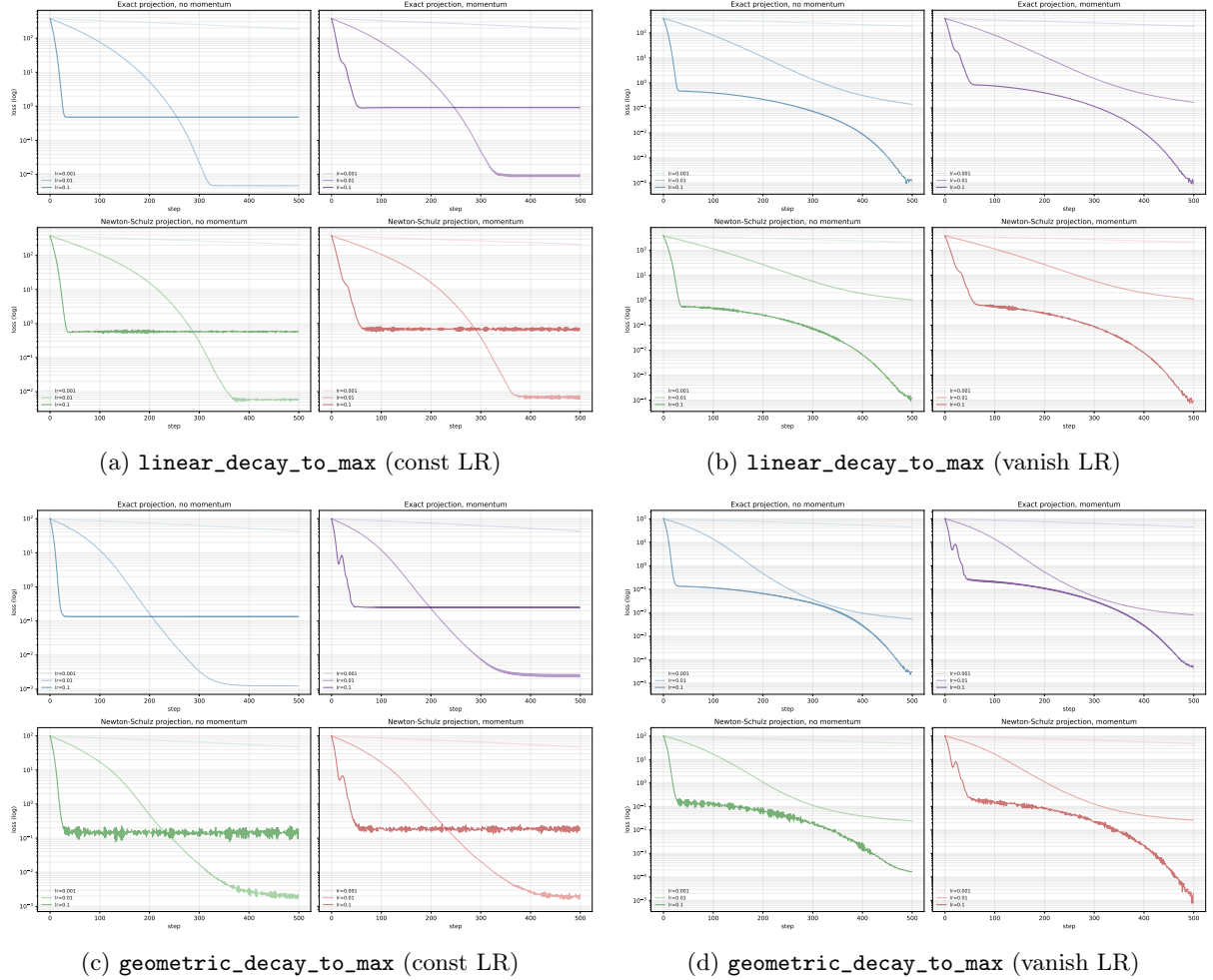


Figure 12: Sample trajectories for decaying-spectrum families (same setting as Figure 10).

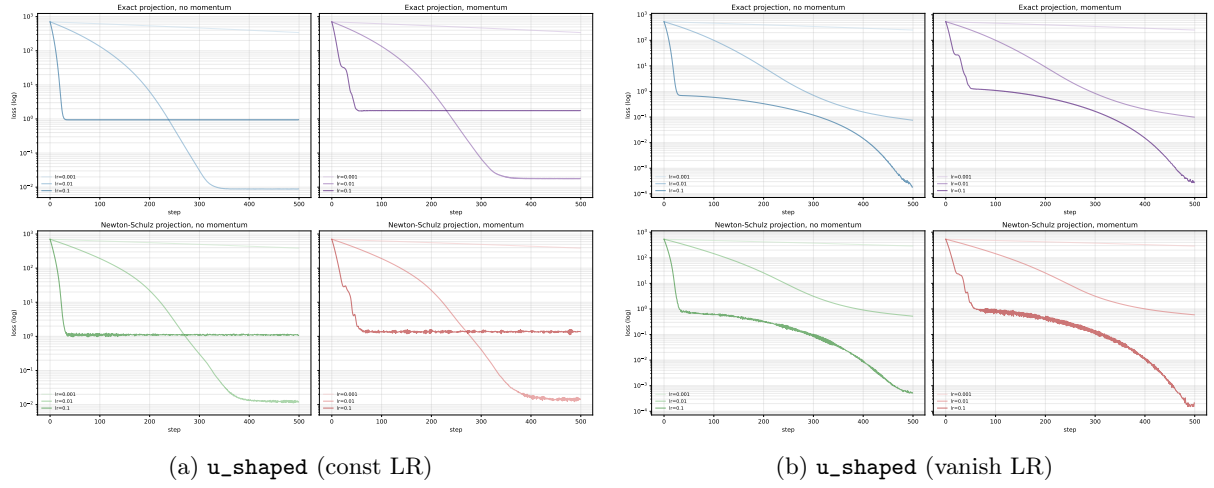


Figure 13: Sample trajectories for the  $u_{\text{shaped}}$  spectrum (same setting as Figure 10).

## D.7 Gradient-conditioning diagnostics

Some practitioner discussions refer to “conditioning of the gradients along training” rather than Hessian conditioning. We report the averaged gradient condition numbers in our controlled-spectrum experiments in Figures 14–15, together with the averaged loss trajectories. The qualitative conclusion matches Section 3.3. Across spectrum families, similar gradient-conditioning profiles along classical GD can

correspond to qualitatively different benefits when switching to MUON. For instance, the condition number profiles for `geometric_decay_to_max` and `uniform` spectra are similarly decreasing from  $10^8$  to  $10^7$  (first two rows in Figure 15), yet switching to MUON is only beneficial for the `geometric_decay_to_max` case (Table 1). This suggests that the gradient conditioning measure alone does not explain the relative speed of GD and MUON on these quadratics.

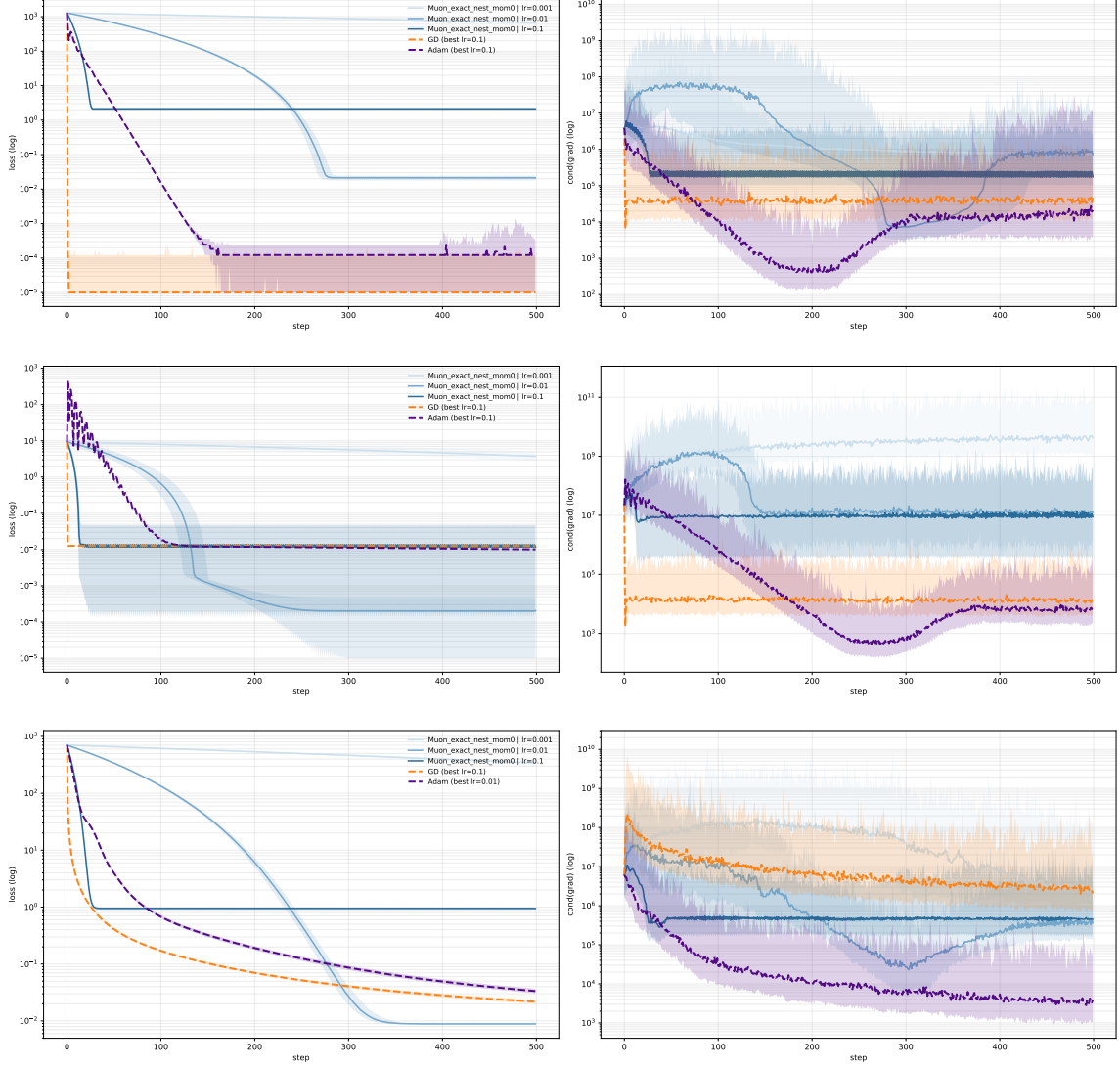


Figure 14: Averaged trajectories for `max_spiked` (top), `min_spiked` (middle), and `u_shaped` (bottom) spectra. Each panel shows the loss curves (left) and the gradient conditioning measure along the trajectory (right), averaged over random initializations.

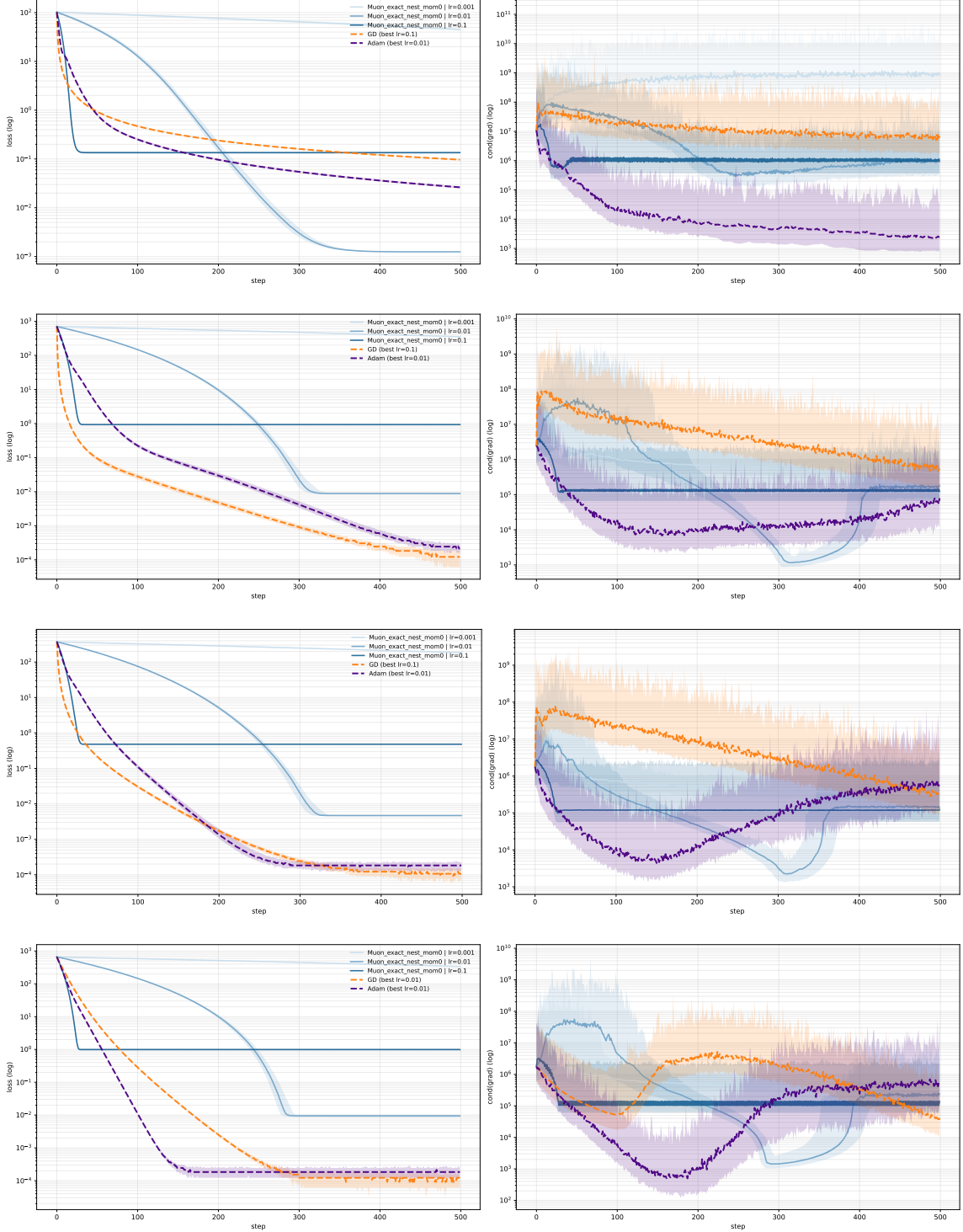


Figure 15: Averaged trajectories for `geometric_decay_to_max` (top), `uniform` (second), `linear_decay_to_max` (third), and `gaussian` (bottom) spectra. Each panel shows the loss curves (left) and the gradient conditioning measure along the trajectory (right), averaged over random initializations. Gradient conditioning alone does not predict which method converges faster.

## E Noisy Sign Dynamics Results

In this appendix, we analyze the one-dimensional noisy sign dynamics of Equation (10). We use a different notation than in the main text: time is indexed by  $n$  instead of  $t$ , and the state of the process at time  $n$  with noise level  $\sigma \geq 0$  is denoted by  $w_n^{(\sigma)}$  rather than  $s_t^{(\sigma)}$ .

**Proposition E.1** (Noise breaks the deterministic grid trap). *Consider the one-dimensional noisy sign dynamics with step size  $\alpha > 0$  and noise level  $\sigma \geq 0$ :*

$$w_{n+1}^{(\sigma)} = w_n^{(\sigma)} - \alpha(\text{sign}(w_n^{(\sigma)}) + \sigma \xi_{n+1}), \quad n \geq 0,$$

where  $(\xi_n)_{n \geq 1}$  are i.i.d.  $\mathcal{N}(0, 1)$  random variables and  $w_0^{(\sigma)} \in \mathbb{R}$  is fixed.

Fix  $\varepsilon > 0$  and define the hitting time

$$T_\varepsilon^{(\sigma)} := \inf\{n \geq 0 : |w_n^{(\sigma)}| \leq \varepsilon\}. \quad (19)$$

Assume  $\sigma > 0$ . Then, for any initialization  $w_0 \in \mathbb{R}$ ,

$$\mathbb{P}(T_\varepsilon^{(\sigma)} < \infty) = 1.$$

By contrast, for the deterministic dynamics ( $\sigma = 0$ ), if the grid  $w_0 + \alpha \mathbb{Z}$  does not intersect  $[-\varepsilon, \varepsilon]$ , then  $T_\varepsilon^{(0)} = \infty$  for all such initializations.

*Proof idea for Theorem E.1.* (Full proof in Section E.1.) The proof combines a drift-to-compact argument with a uniform ‘attempt’ mechanism: once the process enters a fixed neighborhood of the origin, there is a state-uniform positive probability to land in  $[-\varepsilon, \varepsilon]$  within a bounded number of steps, and repeated returns to that neighborhood (which happen almost surely because of the drift) guarantee eventual success.  $\square$

**Proposition E.2** (Small- and large-noise have long hitting times). *Assume the deterministic iteration  $w_{n+1}^{(0)} = w_n^{(0)} - \alpha \text{sign}(w_n^{(0)})$  satisfies  $|w_n^{(0)}| \geq \varepsilon + \Delta, \forall n \geq 0$ , for some margin  $\Delta > 0$ ; that is, the step grid misses the target interval. Consider, for  $\sigma \geq 0$ ,*

$$w_{n+1}^{(\sigma)} = w_n^{(\sigma)} - \alpha(\text{sign}(w_n^{(\sigma)}) + \sigma \xi_{n+1}), \quad w_0^{(\sigma)} = w_0,$$

where  $(\xi_n)$  are i.i.d. standard Gaussian random variables.

Let  $T_\varepsilon^{(\sigma)}$  denote the hitting time of  $[-\varepsilon, \varepsilon]$  as in (19). For any positive integer  $N$ , we have

$$\lim_{\sigma \rightarrow 0} \mathbb{P}(T_\varepsilon^{(\sigma)} > N) = \lim_{\sigma \rightarrow \infty} \mathbb{P}(T_\varepsilon^{(\sigma)} > N) = 1.$$

*Proof idea for Theorem E.2.* (Full proof in Section E.2.) Informally, for very small noise the process shadows the deterministic two-cycle for a long time before accumulated fluctuations are large enough to sufficiently escape the lattice and hit the target interval. For very large noise, the update becomes dominated by the random term  $\sigma \xi_{n+1}$ , and the chain behaves like a rapidly diffusing random walk whose steps are so large that it frequently overshoots the small target interval  $[-\varepsilon, \varepsilon]$ .  $\square$

## E.1 Proof of Theorem E.1

The case  $\sigma = 0$  is clear since the dynamics live on the grid  $w_0 + \alpha \mathbb{Z}$ , so if that grid misses  $[-\varepsilon, \varepsilon]$  then the process never hits that interval. Now, fix  $\sigma > 0$ .

**Step 1: a drift-to-compact lemma.** We show that there exists  $R > 0$  such that, for any starting point  $w_0^{(\sigma)}$ , the hitting time

$$\tau_R := \inf\{n \geq 0 : |w_n^{(\sigma)}| \leq R\}$$

is almost surely finite.

It suffices to prove that there exist constants  $R > 0$  and  $\delta > 0$  such that, for all  $|w| \geq R$ ,

$$\mathbb{E}\left[|w_1^{(\sigma)}| - |w_0^{(\sigma)}| \mid w_0^{(\sigma)} = w\right] \leq -\delta. \quad (20)$$

Indeed, let  $\mathcal{F}_n := \sigma(\xi_1, \dots, \xi_n)$  be the natural filtration, and consider the stopped process

$$Z_n := |w_{\min(n, \tau_R)}^{(\sigma)}| + \delta \min(n, \tau_R).$$

We claim that  $\mathbb{E}[Z_{n+1} \mid \mathcal{F}_n] \leq Z_n$  for all  $n \geq 0$ , i.e.,  $(Z_n)_{n \geq 0}$  is a supermartingale with respect to  $(\mathcal{F}_n)_{n \geq 0}$ .

To see this, consider the two cases:

- On the event  $\{\tau_R \leq n\}$ , the process is already stopped, so  $Z_{n+1} = Z_n$  and

$$\mathbb{E}[Z_{n+1} \mathbf{1}_{\{\tau_R \leq n\}} \mid \mathcal{F}_n] = \mathbb{E}[Z_n \mathbf{1}_{\{\tau_R \leq n\}} \mid \mathcal{F}_n] = Z_n \mathbf{1}_{\{\tau_R \leq n\}}.$$

since  $\{\tau_R \leq n\}$  is  $\mathcal{F}_n$ -measurable.

- On the event  $\{\tau_R > n\}$ , we have  $\min(n+1, \tau_R) = n+1$  so that pointwise

$$Z_{n+1} - Z_n = \mathbf{1}_{\{\tau_R > n\}} \left( |w_{n+1}^{(\sigma)}| - |w_n^{(\sigma)}| + \delta \right).$$

Taking conditional expectation given  $\mathcal{F}_n$  and using that  $\mathbf{1}_{\{\tau_R > n\}}$  is  $\mathcal{F}_n$ -measurable,

$$\mathbb{E}[Z_{n+1} - Z_n \mid \mathcal{F}_n] = \mathbf{1}_{\{\tau_R > n\}} \left( \mathbb{E}[|w_{n+1}^{(\sigma)}| - |w_n^{(\sigma)}| \mid \mathcal{F}_n] + \delta \right).$$

Define the one-step update map

$$\Phi(x, u) := x - \alpha(\text{sign}(x) + \sigma u),$$

so that  $w_{n+1}^P = \Phi(w_n, \xi_{n+1})$ , where we omit the superscript  $(\sigma)$  for brevity.

Let  $g : \mathbb{R} \rightarrow \mathbb{R}$  be any measurable function with  $\mathbb{E}|g(w_{n+1})| < \infty$ . Since  $w_n$  is  $\mathcal{F}_n$ -measurable, and  $\xi_{n+1}$  is independent of  $\mathcal{F}_n$  with the same distribution as  $\xi_1$ , we have:

$$\mathbb{E}[g(w_{n+1}) \mid \mathcal{F}_n] = \psi_g(w_n) \quad \text{a.s.}, \quad \psi_g(x) := \mathbb{E}[g(\Phi(x, \xi_1))] = \mathbb{E}[g(w_1) \mid w_0 = x]. \quad (21)$$

Applying (21) with  $g(y) = |y|$ , we get

$$\mathbb{E}[|w_{n+1}| - |w_n| \mid \mathcal{F}_n] = \mathbb{E}[|w_1| - |w_0| \mid w_0 = w_n]$$

The event  $\{n < \tau_R\}$  is  $\mathcal{F}_n$ -measurable and implies  $|w_n| > R$ . Therefore, on  $\{n < \tau_R\}$  we may apply (20) at the (random) starting point  $w = w_n$ :

$$\mathbb{E}[|w_1| - |w_0| \mid w_0 = w_n] \leq -\delta.$$

This yields

$$\mathbf{1}_{\{n < \tau_R\}} \mathbb{E}[|w_{n+1}| - |w_n| \mid \mathcal{F}_n] \leq -\delta \mathbf{1}_{\{n < \tau_R\}}.$$

Combining the two cases, we get  $\mathbb{E}[Z_{n+1} \mid \mathcal{F}_n] \leq Z_n$ . Taking expectations yields  $\mathbb{E}[Z_{n+1}] \leq \mathbb{E}[Z_n] \leq \dots \leq \mathbb{E}[Z_0] = |w_0^{(\sigma)}|$ . In particular,  $\delta \mathbb{E}[\min(n, \tau_R)] \leq \mathbb{E}[Z_n] \leq |w_0^{(\sigma)}|$  for all  $n \geq 0$ . Letting  $n \rightarrow \infty$  and using monotone convergence gives  $\mathbb{E}[\tau_R] = \lim_{n \rightarrow \infty} \mathbb{E}[\min(n, \tau_R)] \leq |w_0^{(\sigma)}|/\delta < \infty$ , hence  $\mathbb{P}(\tau_R < \infty) = 1$ .

We now verify (20). We keep omitting the superscript  $(\sigma)$  for brevity. Let  $\Delta := \alpha(1 + \sigma \xi_1)$ . By symmetry it suffices to consider starting at  $w > 0$ , in which case  $w_1 = w - \Delta$  and

$$|w_1| = |w - \Delta| = (w - \Delta) + 2(\Delta - w)_+, \quad (a)_+ := \max(0, a).$$

Taking expectations over the centered noise  $\xi_1$ , we have  $\mathbb{E}[\Delta] = \alpha$  and thus

$$\mathbb{E}[|w_1| \mid w_0 = w] = w - \alpha + 2 \mathbb{E}[(\Delta - w)_+]. \quad (22)$$

We claim that  $\mathbb{E}[(\Delta - w)_+] \rightarrow 0$  as  $w \rightarrow \infty$ . For  $w \geq 1$ , define  $g_w(\Delta) := (\Delta - w)_+$ . Then  $g_w(\Delta) \downarrow 0$  pointwise if  $w \rightarrow \infty$  and  $0 \leq g_w(\Delta) \leq \Delta_+$ , where  $\mathbb{E}[\Delta_+] < \infty$  since  $\Delta$  is Gaussian. By dominated convergence,  $\mathbb{E}[(\Delta - w)_+] \rightarrow 0$ .

Therefore we may choose  $R$  large enough so that for all  $w \geq R$ ,  $2 \mathbb{E}[(\Delta - w)_+] \leq \alpha/2$ . Plugging this into (22) yields

$$\mathbb{E}[|w_1| \mid w_0 = w] \leq w - \alpha/2 \quad (\forall w \geq R),$$

and by symmetry the same bound holds for  $w \leq -R$ . Thus (20) holds with  $\delta := \alpha/2$ .

**Step 2: a uniform bounded-noise contraction window.** We now show that starting from any  $|w_0^{(\sigma)}| \leq R$ , there is a positive probability of hitting  $[-\varepsilon, \varepsilon]$  in a fixed number of steps which does not depend on the starting point.

Pick any  $M > 0$  such that  $c := \alpha(1 - \sigma M) > 0$ . Fix  $n \geq 0$ . On the event  $\{|\xi_{n+1}| \leq M\}$  we have

$$w_{n+1}^{(\sigma)} \leq w_n^{(\sigma)} - c \text{ if } w_n^{(\sigma)} > 0, \quad w_{n+1}^{(\sigma)} \geq w_n^{(\sigma)} + c \text{ if } w_n^{(\sigma)} < 0, \quad (23)$$

i.e., the process moves towards zero by at least  $c$  in that case. In  $L$  steps, this ensures a movement of at least  $Lc$  towards zero. If  $L > R/c$ , starting from  $|w_0^{(\sigma)}| \leq R$  and with  $|\xi_1|, \dots, |\xi_L| \leq M$ , the process must cross the level  $\pm\varepsilon$  for some  $n \leq L$ . At the crossing time, since the one-step move is at most

$$|w_n^{(\sigma)} - w_{n-1}^{(\sigma)}| = \alpha|1 + \sigma\xi_n| \leq \alpha(1 + \sigma M) =: C, \quad (24)$$

the pre-crossing iterate lies in  $[-\varepsilon - C, \varepsilon + C]$ . We now show that from there, there is a positive probability of landing in  $[-\varepsilon, \varepsilon]$  at the next step.

Define the compact interval  $B := [-\varepsilon - C, \varepsilon + C]$ . For any  $x \in B$ , the one-step transition is

$$w_1^{(\sigma)} = x - \alpha \text{sign}(x) - \alpha\sigma\xi_1,$$

so  $w_1^{(\sigma)}$  has a Gaussian density with variance  $(\alpha\sigma)^2$ . Hence  $\mathbb{P}_x(w_1^{(\sigma)} \in [-\varepsilon, \varepsilon]) > 0$  for every  $x \in B$ . Moreover,  $x \mapsto \mathbb{P}_x(w_1^{(\sigma)} \in [-\varepsilon, \varepsilon])$  is continuous (it can be expressed in terms of Gaussian CDFs), so by compactness,

$$p' := \inf_{x \in B} \mathbb{P}_x(w_1^{(\sigma)} \in [-\varepsilon, \varepsilon]) > 0.$$

Consequently, defining  $L_R := \lceil R/c \rceil$ ,  $p := \mathbb{P}(|\xi_1| \leq M, \dots, |\xi_{L_R-1}| \leq M) > 0$ , and

$$q := p^{L_R} p' \in (0, 1),$$

we just showed that on the event  $\{|\xi_1| \leq M, \dots, |\xi_{L_R-1}| \leq M\}$ , starting from any  $x$  with  $|x| \leq R$ , we reach  $[-\varepsilon, \varepsilon]$  with probability at least  $q$  in  $L_R$  steps:

$$\inf_{|x| \leq R} \mathbb{P}\left(\exists n \in \{1, \dots, L_R\} : w_n^{(\sigma)} \in [-\varepsilon, \varepsilon] \mid w_0^{(\sigma)} = x\right) \geq q. \quad (25)$$

**Step 3: successive attempts and independence.** We now combine the two previous steps to show that  $T_\varepsilon^{(\sigma)} < \infty$  almost surely: we repeatedly wait for the process to return to  $[-R, R]$  (which happens a.s. by Step 1), then we make an attempt of length  $L_R$  to hit  $[-\varepsilon, \varepsilon]$ . Each attempt succeeds with probability at least  $q$  independently of the past, so eventually one attempt must succeed a.s.

Define the successive *attempt start times*  $(S_k)_{k \geq 0}$  and end times  $T_k := S_k + L_R$  recursively by

$$S_0 := \tau_R, \quad S_{k+1} := \inf\{n \geq T_k : |w_n^{(\sigma)}| \leq R\}, \quad T_k := S_k + L_R.$$

**Claim:**  $S_k < \infty$  a.s. for all  $k$ . We prove this by induction. Step 1 gives  $S_0 = \tau_R < \infty$  a.s. Assume  $S_k < \infty$  a.s. for some  $k$ . Then  $T_k = S_k + L_R < \infty$  a.s. as well. On the event  $\{T_k < \infty\}$ , apply the strong Markov property at time  $T_k$ : conditionally on  $\mathcal{F}_{T_k}$  (the sigma-algebra generated by  $(\xi_1, \dots, \xi_{T_k})$  [Le Gall, 2022, Def 12.8]), the post- $T_k$  chain  $(w_{T_k+n}^{(\sigma)})_{n \geq 0}$  has the same law as the chain started from  $w_{T_k}^{(\sigma)}$ . In particular,

$$\mathbb{P}(S_{k+1} < \infty \mid \mathcal{F}_{T_k}) = \mathbb{P}_{w_{T_k}^{(\sigma)}}(\tau_R < \infty) \quad \text{a.s. on } \{T_k < \infty\}.$$

Since Step 1 holds for *any* initial condition, we have  $\mathbb{P}_x(\tau_R < \infty) = 1$  for every  $x \in \mathbb{R}$ , hence

$$\mathbb{P}(S_{k+1} < \infty \mid \mathcal{F}_{T_k}) = 1 \quad \text{a.s.}$$

Taking expectations yields  $\mathbb{P}(S_{k+1} < \infty) = 1$ , completing the induction.

To conclude the proof, we now show that at least one attempt succeeds a.s. The argument essentially relies on the conditional independence of the attempts  $A_k$  defined below.

For each  $k$ , consider the event that the  $k$ -th attempt succeeds:

$$A_k := \left\{ \exists n \in \{S_k + 1, \dots, T_k\} : w_n^{(\sigma)} \in [-\varepsilon, \varepsilon] \right\}.$$

It depends only on  $(\xi_{S_k+1}, \dots, \xi_{T_k})$  and on  $w_{S_k}^{(\sigma)}$ . Conditioned on  $\mathcal{F}_{S_k}$ , the noises  $(\xi_{S_k+1}, \dots, \xi_{T_k})$  are independent of  $\mathcal{F}_{S_k}$  and i.i.d. Gaussian, hence by Strong Markov property and (25),

$$\mathbb{P}(A_k \mid \mathcal{F}_{S_k}) \geq q \quad \text{a.s.} \quad (26)$$

Note that  $\mathbb{P}(A_k \mid \mathcal{F}_{S_k})$  is an  $\mathcal{F}_{S_k}$ -measurable random variable (a conditional success probability given the past up to time  $S_k$ ). Therefore,

$$\mathbb{P}\left(\bigcap_{k=0}^N A_k^c\right) = \mathbb{E}\left[\prod_{k=0}^N \mathbb{P}(A_k^c \mid \mathcal{F}_{S_k})\right] \leq (1-q)^{N+1}.$$

Letting  $N \rightarrow \infty$  yields

$$\mathbb{P}\left(\forall k \geq 0, A_k^c\right) = 0,$$

so with probability one, some attempt succeeds, i.e.,  $T_\varepsilon^{(\sigma)} < \infty$  almost surely. This proves  $\mathbb{P}(T_\varepsilon^{(\sigma)} < \infty) = 1$ .

## E.2 Proof of Theorem E.2

We treat the small-noise and large-noise regimes separately.

**Small-noise regime**  $\sigma \rightarrow 0$ . Fix  $N > 0$ , consider  $S_n := \sum_{k=1}^n \xi_k$ , and define the event

$$A_\sigma := \left\{ \max_{1 \leq n \leq N} |\sigma S_n| \leq \frac{\Delta}{2\alpha} \right\}.$$

We claim that on  $A_\sigma$  the noisy and deterministic iterates have the same sign up to time  $N$  if they start from the same initialization:

$$w_n^{(\sigma)} - w_n^{(0)} = -\alpha\sigma S_n \quad \text{for all } n \leq N. \quad (27)$$

Indeed, argue by induction. For  $n = 0$  it is trivial. Assume the signs agree up to time  $n - 1$ . Then (27) holds at time  $n - 1$ , so on  $A_\sigma$  we have

$$|w_{n-1}^{(\sigma)} - w_{n-1}^{(0)}| \leq \frac{\Delta}{2}.$$

Since  $|w_{n-1}^{(0)}| \geq \varepsilon + \Delta$  by assumption, this implies  $\text{sign}(w_{n-1}^{(\sigma)}) = \text{sign}(w_{n-1}^{(0)})$ , completing the induction. Therefore, on  $A_\sigma$ , for all  $n \leq N$ ,

$$|w_n^{(\sigma)}| \geq |w_n^{(0)}| - \alpha\sigma|S_n| \geq (\varepsilon + \Delta) - \frac{\Delta}{2} = \varepsilon + \frac{\Delta}{2} > \varepsilon,$$

so  $T_\varepsilon^{(\sigma)} > N$  on  $A_\sigma$ , and thus

$$\mathbb{P}(T_\varepsilon^{(\sigma)} \leq N) \leq \mathbb{P}(A_\sigma^c).$$

By Kolmogorov's inequality and  $\mathbb{E}[\xi_1^2] = 1$ ,

$$\mathbb{P}(A_\sigma^c) = \mathbb{P}\left(\max_{1 \leq n \leq N} |S_n| > \frac{\Delta}{2\alpha\sigma}\right) \leq \frac{N}{(\Delta/(2\alpha\sigma))^2} = O(\sigma^2),$$

which tends to 0 as  $\sigma \rightarrow 0$ . Hence

$$\mathbb{P}(T_\varepsilon^{(\sigma)} > N) \rightarrow 1 \quad \text{as } \sigma \rightarrow 0.$$

**Large-noise regime**  $\sigma \rightarrow \infty$ . Fix  $N > 0$ . By a union bound,

$$\mathbb{P}(T_\varepsilon^{(\sigma)} \leq N) \leq \sum_{k=1}^N \mathbb{P}(|w_k^{(\sigma)}| \leq \varepsilon).$$

Let  $\mathcal{F}_{k-1}$  be the natural filtration up to time  $k - 1$ . Since

$$w_k^{(\sigma)} = w_{k-1}^{(\sigma)} - \alpha \text{sign}(w_{k-1}^{(\sigma)}) - \alpha\sigma\xi_k,$$

we have, conditionally on  $\mathcal{F}_{k-1}$ ,

$$w_k^{(\sigma)} | \mathcal{F}_{k-1} \sim \mathcal{N} \left( w_{k-1}^{(\sigma)} - \alpha \text{sign}(w_{k-1}^{(\sigma)}), \alpha^2 \sigma^2 \right).$$

Thus, almost surely, the conditional probability  $\mathbb{P}(|w_k^{(\sigma)}| \leq \varepsilon | \mathcal{F}_{k-1})$  (a random variable conditioned on the past up to time  $k-1$ ) can be expressed in terms of the Gaussian density as

$$\mathbb{P}(|w_k^{(\sigma)}| \leq \varepsilon | \mathcal{F}_{k-1}) = \int_{-\varepsilon}^{\varepsilon} \frac{1}{\alpha \sigma \sqrt{2\pi}} \underbrace{\exp \left( -\frac{(y-m)^2}{2\alpha^2 \sigma^2} \right)}_{\leq 1} dy \leq \frac{2\varepsilon}{\alpha \sigma \sqrt{2\pi}},$$

where  $m = w_{k-1}^{(\sigma)} - \alpha \text{sign}(w_{k-1}^{(\sigma)})$  is random. Taking expectations yields

$$\mathbb{P}(|w_k^{(\sigma)}| \leq \varepsilon) \leq \frac{2\varepsilon}{\alpha \sigma \sqrt{2\pi}}.$$

Hence the result:

$$\mathbb{P}(T_\varepsilon^{(\sigma)} \leq N) \leq N \frac{2\varepsilon}{\alpha \sigma \sqrt{2\pi}} \xrightarrow[\sigma \rightarrow \infty]{} 0.$$

## F Experiments on Noisy Sign Dynamics

### F.1 1D toy model experiments

Figure 4 has been generated as follows. We simulate (10) with i.i.d. standard Gaussian noise  $\xi_t \sim \mathcal{N}(0, 1)$  and parameters

$$\alpha = 0.1, \quad \varepsilon = \frac{\alpha}{5}, \quad s_0 = 10\alpha + 1.3\varepsilon.$$

The choice of  $s_0$  ensures that the exact sign dynamics never hit  $[-\varepsilon, \varepsilon]$ . For each noise level  $\sigma$  on a logarithmic grid (from  $10^{-3}$  to 10) we run  $n_{\text{samples}} = 10^4$  independent trajectories, cap the simulation at  $n_{\text{max}} = 1000$  steps, and measure  $\tilde{T} := \min(T_\varepsilon^{(\sigma)}, n_{\text{max}})$ . We compute the median of  $\tilde{T}$  over the  $n_{\text{samples}}$  trajectories, and its [2.5%, 97.5%] empirical quantile interval. These are plotted in Figure 4 (the quantile interval is shaded in light blue).

### F.2 Newton–Schulz approximate error vs. exact projection on controlled-spectrum quadratics

Table 8 complements Table 2 by reporting the best-loss ratios for MUON with Newton–Schulz projection (no momentum) vs. MUON with exact projection (no momentum) on the same controlled-spectrum quadratic instances as in Table 2. It shows that Newton–Schulz MUON attains a loss within a factor 2 of exact-projection MUON on most spectrum families and time horizons, except on `min_spiked`, where Newton–Schulz is significantly better.

Table 8: Mean  $\pm 1.96$  standard error (over initializations) of best-loss for MUON with exact projection, divided by best-loss for MUON with Newton–Schulz projection (no momentum, constant step size). Values  $> 1$  favor Newton–Schulz. This can be read as “Newton–Schulz MUON is better by a factor of `value` on average”.

kind	$t = T/10$	$t = T/2$	$t = T$
<code>max_spiked</code>	$0.61 \pm 0.016488$	$0.48 \pm 0.025829$	$1.15 \pm 0.020648$
<code>min_spiked</code>	$1.32 \pm 0.275357$	$8.58 \pm 3.246216$	$33.18 \pm 8.962830$
<code>uniform</code>	$0.36 \pm 0.003587$	$0.71 \pm 0.012810$	$0.71 \pm 0.003194$
<code>gaussian</code>	$0.40 \pm 0.003579$	$0.55 \pm 0.023125$	$0.81 \pm 0.005050$
<code>linear_decay_to_max</code>	$0.33 \pm 0.002264$	$0.82 \pm 0.004592$	$0.78 \pm 0.003515$
<code>u_shaped</code>	$0.46 \pm 0.003740$	$0.42 \pm 0.012617$	$0.71 \pm 0.004944$
<code>geometric_decay_to_max</code>	$0.58 \pm 0.007069$	$0.21 \pm 0.006506$	$0.83 \pm 0.008606$

## G Exact line search on a quadratic: formulas and additional plots

This appendix records the exact line-search expressions used in Section 5 and provides additional trajectory-level plots for the same quadratic instance.

**Quadratic model.** We consider the quadratic loss

$$L(W) = \frac{1}{2} \langle W, AW \rangle, \quad A \succ 0, \quad (28)$$

with Frobenius inner product  $\langle X, Y \rangle = \text{trace}(X^\top Y)$ . The unique minimizer is  $W_\star = 0$ , and the gradient is

$$\nabla L(W) = AW. \quad (29)$$

**Exact line search along a direction.** Fix an iterate  $W$  and a direction  $D$ . Along the ray  $W - \alpha D$ ,

$$L(W - \alpha D) = L(W) - \alpha \langle \nabla L(W), D \rangle + \frac{1}{2} \alpha^2 \langle D, AD \rangle. \quad (30)$$

Since  $A \succ 0$ , we have  $\langle D, AD \rangle > 0$  for any  $D \neq 0$ , and the exact line-search minimizer over  $\alpha \in \mathbb{R}$  is

$$\alpha^*(D) = \frac{\langle \nabla L(W), D \rangle}{\langle D, AD \rangle}. \quad (31)$$

Plugging (31) into (30) yields the exact one-step decrease

$$\Delta(D) = L(W) - L(W - \alpha^*(D)D) = \frac{\langle \nabla L(W), D \rangle^2}{2 \langle D, AD \rangle}. \quad (32)$$

**Directions and greedy policy.** As in Section 5, we compare:

$$D_{\text{GD}}(W) = \nabla L(W), \quad D_{\text{St}}(W) = \mathcal{P}(\nabla L(W)),$$

where  $\mathcal{P}(G) = UV^\top$  denotes the polar factor of  $G = U\Sigma V^\top$ . The greedy policy selects, at each iterate,

$$D_{\text{greedy}}(W) = \begin{cases} D_{\text{GD}}(W), & \text{if } \Delta(D_{\text{GD}}(W)) \geq \Delta(D_{\text{St}}(W)), \\ D_{\text{St}}(W), & \text{otherwise.} \end{cases}$$

and then takes the corresponding (exact line-search) step. In the experiments reported in Section 5, the greedy policy always selects the Stiefel direction along its trajectory, even though the GD trajectory is far better overall.

**Additional trajectory-level plots.** Figure 16 reports the gradient norm  $\|\nabla L(W_t)\|_F$  and the distance to the minimizer  $\|W_t - W_\star\|_F$  for the same quadratic instance as in Figure 5. Consistent with the objective gap results in Figure 5, the one-step superiority of the greedy policy does not translate into better end-to-end convergence in terms of these metrics either.

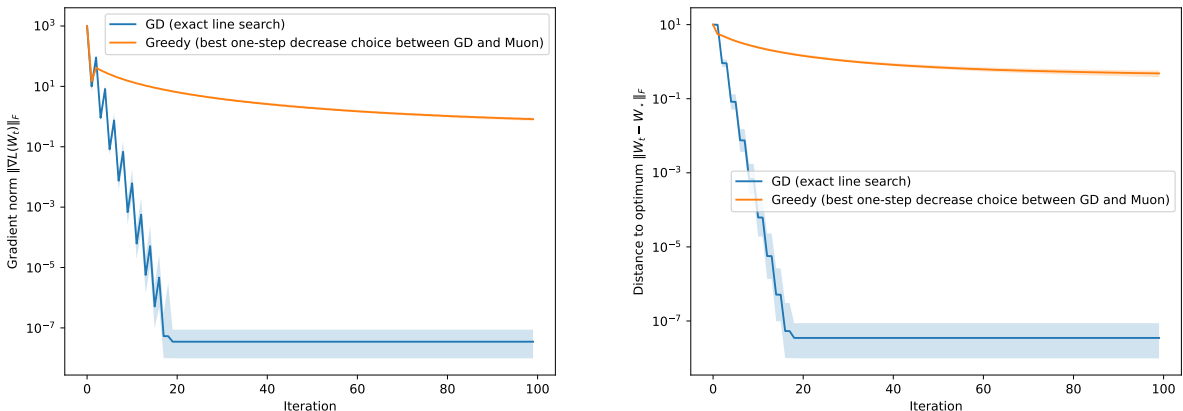


Figure 16: Gradient norm  $\|\nabla L(W_t)\|_F$  (left) and distance to the minimizer  $\|W_t - W_\star\|_F$  (right) for the same quadratic instance as in Figure 5. Results are averaged over 100 random initializations. Shaded bands contain the central 95% of runs.